Article

Cell Reports

Ex Vivo Expanded 3D Human Kidney Spheres Engraft Long Term and Repair Chronic Renal Injury in Mice

Graphical Abstract

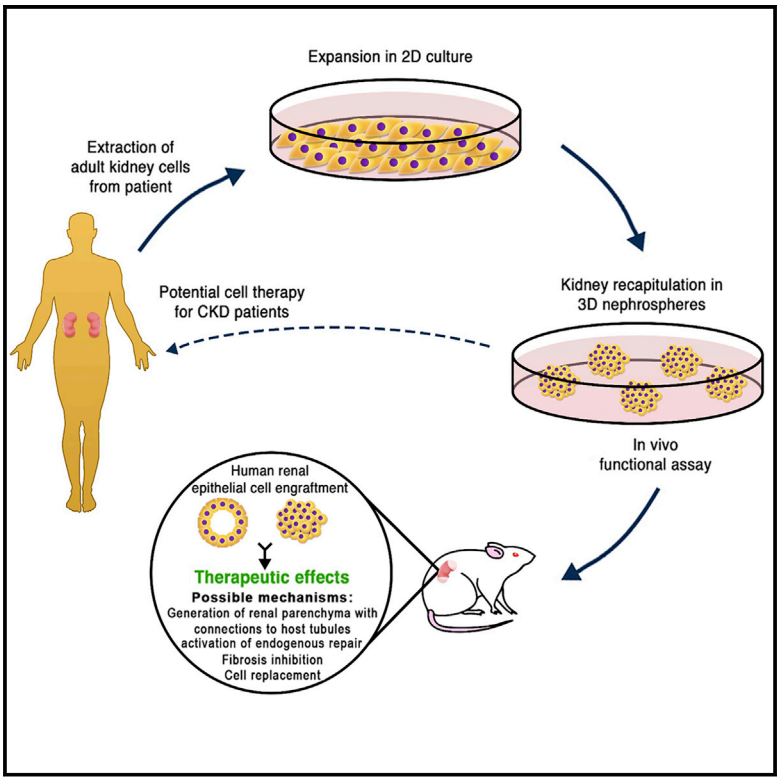

Authors

Orit Harari-Steinberg, Dorit Omer, Yehudit Gnatek, ..., Tomer Kalisky, Zohar Dotan, Benjamin Dekel

Correspondence

binyamin.dekel@sheba.health.gov.il

In Brief

Human kidney cells quickly degenerate in culture, precluding them as a source for cell therapy for chronic kidney disease (CKD). Herein, Harari-Steinberg et al. show that upon culturing as 3D nephrospheres, human kidney cells regain their epithelial phenotype and acquire *in vivo* tissue-forming and reparative properties in a CKD mouse model.

Highlights

- Growing human renal epithelial cells in 3D restores epithelial identity lost in 2D
- These 3D nephrospheres (nSPHs) organize into renal tubular structures *in vivo*
- By doing so, nSPHs engraft long term and improve renal function in CKD mice
- *In vivo* repair involves anti-fibrotic effects and possible addition of nephron segments

Harari-Steinberg et al., 2020, Cell Reports *30*, 852–869
January 21, 2020
https://doi.org/10.1016/j.celrep.2019.12.047

CellPress

OPEN ACCESS
CellPress

Cell Reports
Article

Ex Vivo Expanded 3D Human Kidney Spheres Engraft Long Term and Repair Chronic Renal Injury in Mice

Orit Harari-Steinberg,[1,2,9] Dorit Omer,[1,2,9] Yehudit Gnatek,[1,2,9] Oren Pleniceanu,[1,2] Sanja Goldberg,[1,2] Osnat Cohen-Zontag,[1,2] Sara Pri-Chen,[3] Itamar Kanter,[4] Nissim Ben Haim,[4] Eli Becker,[4] Roi Ankawa,[5] Yaron Fuchs,[5] Tomer Kalisky,[4] Zohar Dotan,[6,7] and Benjamin Dekel[1,2,7,8,10,*]

[1]Pediatric Stem Cell Research Institute, Edmond and Lily Sara Children's Hospital, Sheba Medical Center, Tel Hashomer, Ramat-Gan, Israel
[2]Pediatric Research Center for Genetics, Development and Environment, Sackler School of Medicine, Tel Aviv University, Tel Aviv, Israel
[3]The Maurice and Gabriela Goldschleger Eye Research Institute, Sheba Medical Center, Ramat-Gan, Israel
[4]Faculty of Engineering and Bar-Ilan Institute of Nanotechnology and Advanced Materials (BINA), Bar-Ilan University, Ramat-Gan, Israel
[5]Laboratory of Stem Cell Biology and Regenerative Medicine, Department of Biology, Technion – Israel Institute of Technology, Haifa, Israel
[6]Department of Urology, Sheba Medical Center, Tel Hashomer, Ramat-Gan, Israel
[7]Sackler School of Medicine, Tel Aviv University, Tel Aviv, Israel
[8]Division of Pediatric Nephrology, Safra Children's Hospital, Sheba Medical Center, Ramat-Gan, Israel
[9]These authors contributed equally
[10]Lead Contact
*Correspondence: binyamin.dekel@sheba.health.gov.il
https://doi.org/10.1016/j.celrep.2019.12.047

SUMMARY

End-stage renal disease is a worldwide epidemic requiring renal replacement therapy. Harvesting tissue from failing kidneys and autotransplantation of tissue progenitors could theoretically delay the need for dialysis. Here we use healthy and end-stage human adult kidneys to robustly expand proliferative kidney epithelial cells and establish 3D kidney epithelial cultures termed "nephrospheres." Formation of nephrospheres reestablishes renal identity and function in primary cultures. Transplantation into NOD/SCID mice shows that nephrospheres restore self-organogenetic properties lost in monolayer cultures, allowing long-term engraftment as tubular structures, potentially adding nephron segments and demonstrating self-organization as critical to survival. Furthermore, long-term tubular engraftment of nephrospheres is functionally beneficial in murine models of chronic kidney disease. Remarkably, nephrospheres inhibit pro-fibrotic collagen production in cultured fibroblasts via paracrine modulation, while transplanted nephrospheres induce transcriptional signatures of proliferation and release from quiescence, suggesting re-activation of endogenous repair. These data support the use of human nephrospheres for renal cell therapy.

INTRODUCTION

Chronic kidney disease (CKD) is reaching epidemic proportions in the Western world. CKD in the United States, for example, affects 14% of the population, more than 45 million individuals (National Institute of Diabetes and Digestive and Kidney Diseases, 2016). Therapeutic options are limited to supportive care until end-stage renal disease (stage 5 CKD or ESRD) necessitates dialysis or renal transplantation (Pleniceanu et al., 2010). Worldwide 2 million people are treated with dialysis, and dialysis itself is associated with considerable morbidity and mortality (Liyanage et al., 2015). Kidney transplantation, although offering greater rehabilitation, is limited by severe organ shortages. Two cellular approaches are potentially applicable, the first of which involves bioengineering new kidneys with their delicate architecture and multiple cell types required to generate urine-producing and urine-collecting parts (Shafiee and Atala, 2017). Alternatively, repairing and rejuvenating or regenerating an existing diseased kidney may prevent deterioration of CKD into its terminal phases and thus reduce the need for dialysis or transplantation. A mere 5% change in renal function can differentiate between medical treatment in CKD stage 4 (20% remaining renal function) and dialysis in stage 5 CKD or ESRD (<15% remaining renal function). We previously suggested that renal cell therapy and kidney regeneration and repair using progenitor cell types physiologically intrinsic to kidney development and post-natal growth will be advantageous to cells of non-renal lineages, used for a variety of cellular therapies, such as cord blood cells, mesenchymal stromal cells (MSCs), and hematopoietic stem cells (HSCs) (Dziedzic et al., 2014; Pleniceanu et al., 2010). Importantly, basic understanding of how the kidney develops in embryonic life and how it regenerates its various compartments in adulthood elucidated the precursor cellular lineages that participate in these processes *in vivo* to form new kidney cells and tissues. This in turn allows the selection of what could be ideal renal precursor cell types for the treatment of kidney disease by means of cell therapy (Little et al., 2016; Pleniceanu et al., 2018). In fetal life, a pool of self-renewing multipotent stem cells that reside in a discrete anatomic region, termed the nephrogenic zone, give rise to whole nephrons, which are composed of different types of epithelial cells (Kobayashi

et al., 2008). These cells exist until the 34th week of human gestation, and after that whole new nephrons are no longer formed (Pleniceanu et al., 2018). They can be expanded in specific media and prospectively isolated from human fetal kidneys according to a combination of surface markers, including positive and negative selection (Harari-Steinberg et al., 2013; Pode-Shakked et al., 2016, 2017). Moreover, transplantation of prospectively sorted human developmental renal precursors into mice with progressive renal injury resulted in engraftment of human cells in murine kidneys and in halting the progression of disease (Harari-Steinberg et al., 2013). Nevertheless, with the idea that transplantable committed renal progenitor cells rather than embryonic counterparts or pluripotent stem cel-derived progenitors (Freedman, 2015; Taguchi, 2017) may achieve the fastest route to the clinic, we analyzed the human adult kidney as a possible autologous cell source for kidney repair. The theoretic basis for using the adult kidney stems from clonal lineage tracing showing constant adult kidney growth by renal cells within nephron epithelia that clonally expand to afford tissue replacement over prolonged periods (Rinkevich et al., 2014; Romagnani et al., 2015). Analysis of clonal progeny in steady state and following injury (larger numbers of clones are induced during injury) showed them to be lineage restricted, giving rise to the different anatomic regions of the nephron from which they arise. Thus, the adult kidney replenishes and regenerates its varying tubular compartments in a process that does not require hardwired multipotent stem cells but rather via cells induced to function as committed progenitors for local regeneration. In an attempt to take advantage of the way the adult kidney expands *in vivo*, we analyzed various methods for *ex vivo* cell growth in primary human cultures with the goal of maintaining *in vivo* renal precursor potential. Accordingly, we found that proliferative human adult kidney epithelial cells (hKEpCs), expanded in adherent cultures, form three-dimensional (3D) spheroids (termed nephrospheres [nSPHs]) in serum-free media (Buzhor et al., 2011). Interestingly, when renal cells collected from 3D nSPHs were grafted onto the chorioallantoic membrane of the chick embryo, they showed enhanced potency to generate renal tubular structures within a 1 week time window allowed in the chick model (Buzhor et al., 2011; Noiman et al., 2011). These findings triggered our efforts to comprehensively characterize human nSPHs as well as to study their potency and functionality in a normal and diseased adult mouse environment. Herein, we show that generating human nSPHs entails a genetic program that recapitulates renal development, including mesenchymal-to-epithelial transition (MET) and proliferation-to-quiescence transition, alongside upregulation of tissue-specific genes, so that heterogeneous region-specific renal lineages are represented within nSPHs, renal identity is regained, and renal epithelia is rejuvenated. Human nSPH-derived cells are transplantable in immunodeficient NOD/SCID mice, showing long-term engraftment as self-organizing human 3D tubuloids with putative inter-connections, or less frequently as individual cells within mouse tubules as well as proving to be functionally beneficial in mouse models of CKD. Moreover, we further bridge the gap for translation of autologous renal cell therapy by showing that nSPHs harboring robust renal potential can be developed from a variety of non-functioning end-stage human kidneys. Co-culture experiments of nSPH cells with fibroblasts show paracrine inhibitory effects on collagen synthesis, while a release from quiescence in host mouse tubules following nSPH transplantation is suggestive of activation of an endogenous repair mechanism.

RESULTS

Re-activation of Renal Epithelial Differentiation upon nSPH Formation

We first used RNA sequencing (RNA-seq) to evaluate the sequential transcriptional changes occurring during the generation of 3D nSPHs from expanded two-dimensional (2D) cultures of hKEpCs. The transcriptome of nSPHs originating from three separate human kidneys was analyzed at consecutive time points of 3, 6, and 9 days in 3D conditions (Figure 1; Table S1). Using cluster analysis of temporal transcriptional expression coupled with Gene Ontology analysis, we detected several distinct patterns of transcriptional activity (Figures 1B and 1C; Table S2). These included genes that were upregulated following the transition from 2D to 3D nSPHs, thereafter maintaining constant expression levels (cluster A), genes that following the initial upregulation kept increasing in expression during 3D culture (cluster B), genes that were transiently induced (cluster C), and genes that were initially downregulated and then reached a plateau (cluster D) or continued declining (cluster E). Interestingly, within these clusters we detected significant enrichment for gene families related to renal epithelial development and differentiation (Figure 1B). In Figure 5A and 5B, we found significant enrichment for gene sets denoting differentiation to epithelial segments of the adult kidney. Some examples include epithelial differentiation markers (EPCAM, CDH1, and MUC1), the R-spondin receptor LGR4, and classical segment-specific markers (proximal tubule: SLC34A2; loop of Henle: SLC12A1; distal tubule: SLC12A3; Figure 1B), indicative of epithelial heterogeneity of nSPHs. In fact, a wide array of transporter molecules signifying different compartments of the nephron are enriched in nSPH (Figure S1A). When analyzing cluster C, which denotes gene sets that are initially upregulated but are then downregulated back to baseline levels, we detected genes that characterize early renal developmental stages and developmental progenitors, including metanephric mesenchyme (MM), CM, renal vesicle, and S-shaped body (Magella et al., 2018) (Figure 1B). Clusters D and E include cell cycle and epithelial-to-mesenchymal transition (EMT) gene signature (Figure 1B). When analyzing the mean fold change of each cluster in comparison with baseline levels, we detected that cluster C is activated to a lesser degree compared with clusters A and B, suggesting that the activation of early developmental genes is only to such a degree that allows the activation of more advanced stages of renal development and the expression of genes that are expressed in the mature kidney (Figure 1C). By analyzing the expression pattern of differentially expressed genes related to EMT/MET, we noticed a reduction of EMT-related genes and induction of MET-related genes during nSPH formation (days 3–9) in comparison with hKEpCs (Figure 1D). Additional analysis was performed by defining genes that follow CDH1 (renal differentiation marker) and FZD7 (renal developmental marker) temporal expression patterns and applying gene set enrichment analysis

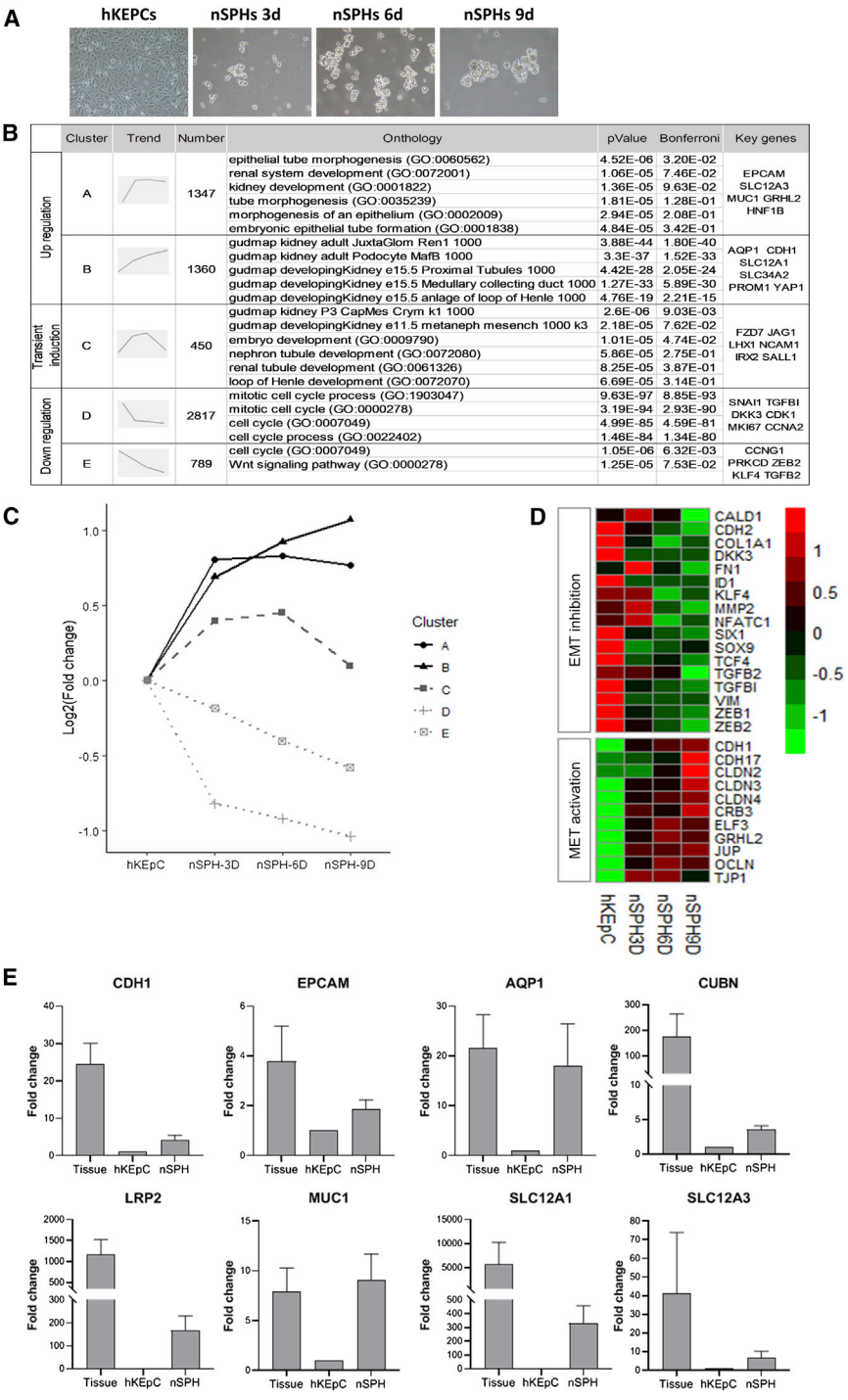

Figure 1. Human nSPHs Recapitulate Epithelial Differentiation

To dissect the transcriptional processes taking place in the transition from 2D culture of hKEpCs to 3D nSPHs, hKEpC were compared with nSPH at three consecutive time points (3, 6, and 9 days in culture). We conducted RNA sequencing analysis to reveal changes in global gene expression.

(A) Phase-contrast microscopic images (10× magnification) of hKEpCs and nSPHs grown for 3, 6, and 9 days.

(B) Table summarizing the different gene clusters found in nSPHs via clustering analysis of RNA-seq data. Cluster A represents genes with similar expression levels in day 3, 6, and 9 nSPHs, which are higher in comparison with hKEpC. Cluster B represents genes whose expression is elevated continuously across time. Cluster C represents genes that are initially upregulated upon the transition to 3D nSPHs but are subsequently downregulated after day 6. Cluster D represents genes with similar expression levels in day 3, 6, and 9 nSPHs, which are lower in comparison with hKEpC. Cluster E represents genes whose expression levels are decreased continuously across time. Gene Ontology (GO) analysis revealed that clusters A and B are enriched for genes related to differentiation to epithelial segments of the adult kidney, cluster C is enriched for early renal developmental genes, and clusters D and E are enriched for genes related to cell cycle and Wnt signaling. Trend, visual demonstration of the expression pattern of the indicated cluster. Number, the number of genes in the indicated cluster. GO analysis was performed using the ToppGene suite; p value and Bonferroni scores relate to the indicated ontology. Key genes, representative genes of each cluster.

(C) Graphic representation of the mean of $\log_2$ fold change ratio at the indicated time point and hKEpCs. Shapes indicate the clusters, colors indicate trend (upregulated, black; transient induction, dark gray; downregulated, light gray).

(D) Heatmap representation of differentially expressed genes related to EMT/MET. Downregulation of EMT-related genes and upregulation of MET-related genes can be detected during nSPH formation (days 3–9) in comparison with hKEpCs.

(E) Quantitative PCR (qPCR) analysis of proximal and distal tubule-specific transcripts in fresh human adult kidney tissue in comparison with cultured epithelial cells as 2D hKEpCs and 3D nSPHs originating from four different kidneys. Renal epithelial cells cultured as nSPH demonstrated significant upregulation of all markers compared with 2D ($p < 0.05$), with expression levels approaching those of fresh tissue, and even demonstrating comparable levels of AQP1 (proximal tubule marker) and MUC1 (distal tubule marker) (the latter as well as EPCAM and SLC12A3 did not reach statistical significance, tissue versus nSPHs). Error bars represent the mean ± SE.

(GSEA). Enriched pathways that followed FZD7 expression in nSPHs included beta-catenin, NOTCH, and TGF-beta. In contrast, for CDH1, GSEA enriched for EMT and cell cycle (c-MYC module) in proliferative hKEpCs, and silencing of these pathways with nSPH formation (Figures S1B and S1C). Altogether, upon culturing in 2D conditions, hKEpCs are released from quiescence, rapidly proliferating and expanding, while leaving behind their *in vivo* renal identity. In contrast, upon generating nSPHs, hKEpCs undergo widespread temporal transcriptional changes, resulting in a recapitulation of renal developmental

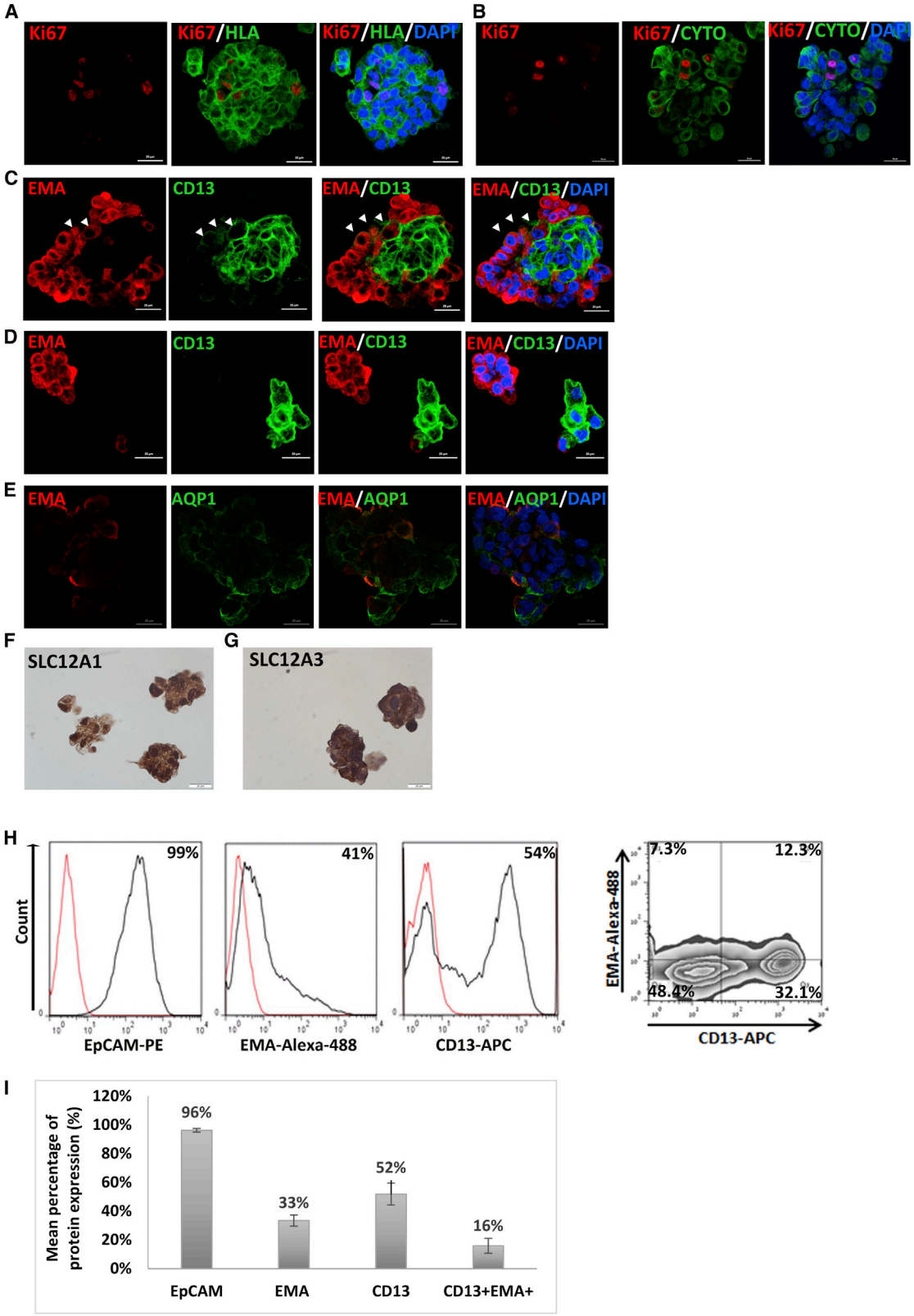

(legend on next page)

programs, followed by MET and differentiation toward a renal epithelial phenotype. Notably, the established transcriptional status supports differentiation toward multiple epithelial lineages, such that the nSPHs recapitulate the epithelial heterogeneity of the adult kidney. Moreover, qRT-PCR comparisons of key functional proximal and distal marker molecules demonstrated significant elevation for all genes in nSPH-cultured cells compared with proliferative hKEpCs (Figure 1E), some of which, such as aquaporin1 (AQP1) and MUC1, attained the levels of fresh human adult kidney tissues from which cultures originated (Figure 1E).

Analysis of the nSPH transcriptome suggested that epithelial programs and functional marker genes are sustained after 1 week in culture. Therefore, for further phenotypic analysis, we used 9 d nSPHs in culture. Although RNA-seq analysis showed significant reduction in cell cycle and proliferation in nSPH, we found that a small proportion of nSPH cells were actively dividing, as demonstrated by nuclear staining of MKi-67, while HLA and cytokeratin positivity indicated human epithelial identity (Figures 2A and 2B). To further analyze renal epithelia in nSPHs, we stained for CD13 (proximal) and EMA (distal) tubular markers. Human-specific and segment-specific staining for these markers was calibrated on sections of human fetal and adult kidneys (Figure S2A). Double staining of nSPHs for CD13/EMA demonstrated cells expressing each of the two markers, as well as bi-phenotypic cells, expressing both CD13 and EMA (Figures 2C and 2D). Interestingly, we also detected the latter subpopulation within the human fetal and adult kidneys (Figures S2B–S2E), indicating that this is a physiological cellular state in human kidneys. Moreover, nSPH epithelia stained positive for AQP1 (proximal), SLC12a1 (loop), and SLC12a3 (distal) transporters (Figures 2E–2G). Flow cytometry analysis for EpCAM, CD13, and EMA confirmed the renal epithelial identity of the nSPHs, as well as the presence of the three types of cellular phenotypes (CD13+, EMA+, and CD13+EMA+ cells) (Figures 2H and 2I). An MSC identity was excluded by the lack of combined high marker expression (CD105, CD90, and CD73). CD45 and CD31 expression levels were similarly low (Table S3). Thus, our two-stage culturing process affords both massive replication and expansion of proliferative hKEpC at the first 2D growth phase, and subsequent re-establishment of renal identity at the protein level upon formation of low-cycling nSPH at the 3D growth stage.

In Vivo Tubular Potential of Human nSPHs in Adult Mice

In order to analyze the *in vivo* renal potential of nSPH, we first established and calibrated a xenotransplantation assay of human renal cells in the subcutaneous (s.c.) space of NOD/SCID mice. This assay entails grafting the human cells within Matrigel, resulting in the formation of a cellular graft, which is removed and analyzed using immunostaining, thereby allowing visualization of engrafted human cells in the mouse background. Cellular grafts attract mouse-derived vessels, as evident by mouse-specific CD31 staining (Figure 3A). Analysis of grafts generated from passage 1 (P1) human nSPH-derived cells (cell suspension dissociated from nSPHs) over periods of 2 and 5 weeks, demonstrated massive engraftment and survival of cells in hosts as self-organizing renal tubular structures, as evident by staining for HLA (Figure 3B). Moreover, improved engraftment was achieved when implanting cells derived from 7 d in comparison with 3 d nSPH cultures (P1), showing an increase in self-organizing renal structures and linking the level of epithelial differentiation in cultured nSPH, shown above by transcriptomics, to their *in vivo* renal potential (Figures 3C–3E). Non-renal lineage cells, such as MSCs, fail to organize and show a scattered engraftment pattern (Figure S3A). Proliferative hKEpCs grown in monolayer engraft as renal structures but exhaust their tubulogenic differentiation potential, resulting in reduced survival in grafts, especially following expansion required for cell up-scaling (Figure S3B). Accordingly, differential renal potency was already noted at P1 so that nSPH-derived cells generated >2-fold more structures (Figures S3C and S3D). Thus, in both monolayer and 3D, survival in the graft mandates self-organization into multicellular tubuloids, rather than as single cells. Because 3D nSPHs exhibit enhanced *in vivo* organogenetic properties, this results in improved post-transplant cell survival. Characteristically, upon implantation into NOD-SCID mice, nSPHs generated tubular structures, exhibiting a patent lumen with either thick or thin epithelial lining (Figure 3F). We subsequently evaluated the 3D nature of the engrafted renal structures using microscopic analysis of the entire graft. We calibrated the HLA staining protocol for whole graft tissue as opposed to analyzing 5 μm slices from paraffin-embedded blocks. This enabled us to capture a 3D view of 200 × 200 × 90 μm by confocal microscopy showing self-organizing 3D human spherical and tubular structures in the mouse background (Figure 3G; Video S1). Accordingly, we demonstrated an elongated tubular organoid of 70–150 μm in length and diameter 25 μm, as well as a spherical structure of 25 μm in diameter (Figure 3G; Video S1). An additional view of 200 × 200 × 50 μm allowed the demonstration of an additional tubular organoid, 160 μm in length and 35 μm in diameter, and a condensate of 75 × 50 × 50 μm (Figure 3G). Further characterization of tubular structures by double staining for Ki-67 and CK

Figure 2. nSPHs Demonstrate Epithelial Characteristics *In Vitro*

(A–D) nSPHs that were grown for 7 days were collected, fixated, stained, and visualized using confocal microscopy. (A) Ki-67 staining shows a minor population of dividing cells. In addition, the nSPHs exhibit an epithelial phenotype, as shown by the expression of cytokeratin (B) and specifically of mature kidney epithelial markers of proximal tubules (CD13; C) and distal tubules (EMA; D). We detected nSPHs composed of both distal and proximal tubular cells (C), as well as nSPHs expressing a single marker (D). Ki-67: Alexa 555, red; HLA: Alexa 488, green; Cyto: Alexa 488, green; DAPI, blue; CD13: Alexa 488, green; EMA: Alexa 555, red; AQP1: Alexa 488; SLC12A1 and SLC12A3-HRP.

(E–G) In addition, nSPH epithelia stained positive for functional molecules: AQP1 (proximal tubule) (E), SLC12a1 (loop of Henle) (F), and SLC12a3 (distal tubule) transporters (G). Scale bars, 20 μm.

(H) Flow cytometry analysis of nSPH cells, demonstrating an epithelial phenotype (EpCAM+). The cells are composed of approximately 40% distal tubular cells (EMA+) and 55% proximal tubular cells (CD13+). Notably, approximately 12.3% of the cells express both markers.

(I) Mean expression levels of the different markers in nSPHs generated from multiple donors: EpCAM (96% ± 1%), EMA (33% ± 4%), CD13 (52% ± 8%), and double-positive staining of EMA and CD13 (16% ± 5%). Error bars represent the mean ± SE.

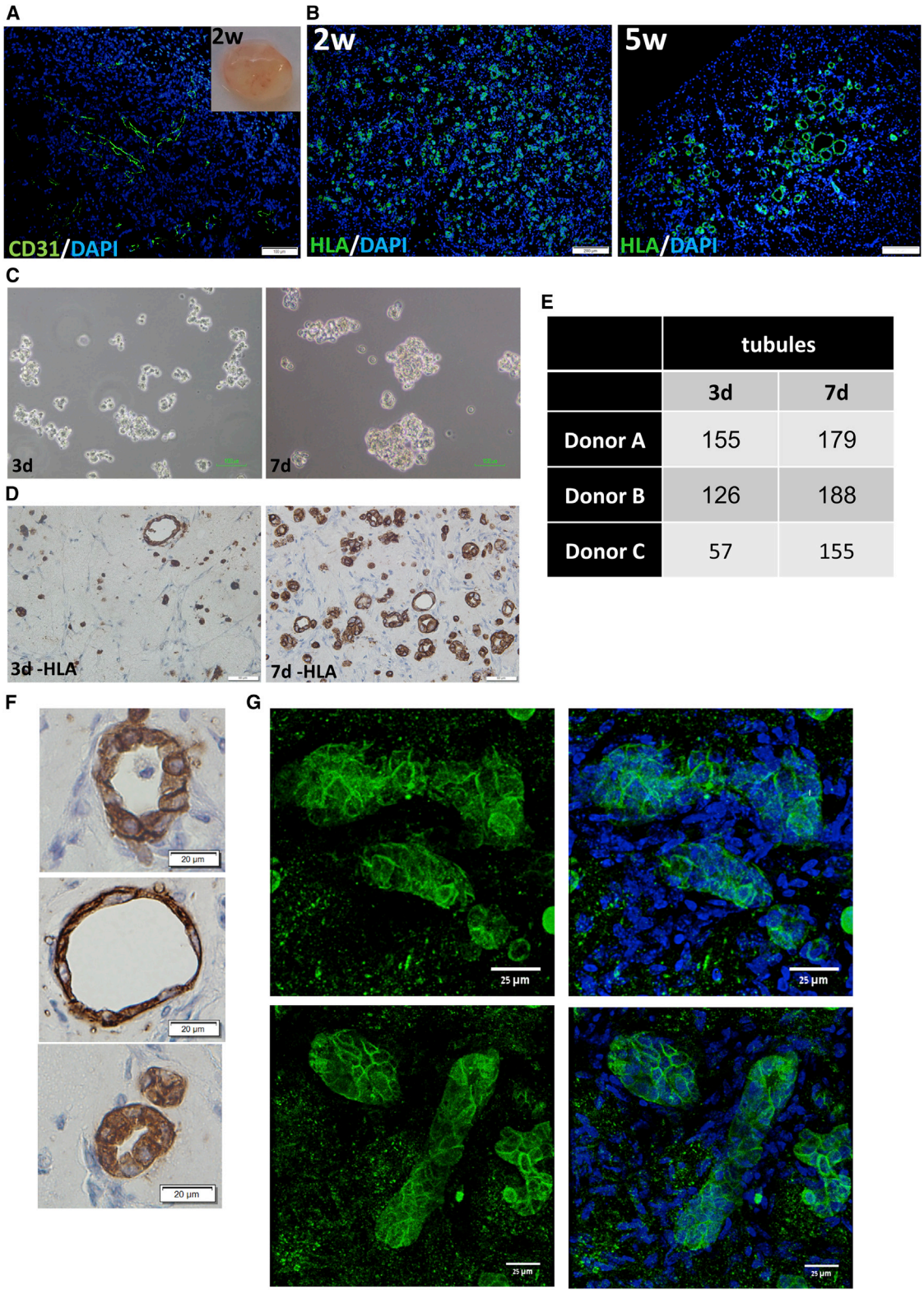

Figure 3. nSPH-Derived Cells Self-Organize to Form Tubule-like Structures *In Vivo*

nSPH-derived cells were suspended in Matrigel and injected subcutaneously into NOD-SCID mice. After 2 weeks, the grafts were harvested and analyzed. (A) Injected nSPH attract mouse blood vessels, as evident both macroscopically (inset) and upon staining for CD31 (green). Scale bars, 100 μm.

(legend continued on next page)

disclosed a small proportion of epithelial cells that are actively dividing (Figure 4A), compatible with *in vivo* adult kidney growth (Rinkevich et al., 2014). Staining with the human-specific CD13/EMA pair disclosed proximal CD13+EMA− and distal EMA+CD13− tubular structures (Figure 4B). In addition to uniphenotypic structures, we also observed structures composed of bi-phenotypic CD13+EMA+ cells (Figure 4B). Of note, in contrast to the pan-membranous CD13 staining seen in cultured nSPHs, established tubular structures *in vivo* demonstrated a shift to luminal staining of CD13, characteristic of the human adult kidney-staining pattern and indicative of acquisition of proper epithelial polarity. Similarly, transporter molecules (AQP1, SLC12A1, and SLC12A3) were apparent in organized structures, which together with the tubular organization and acquisition of cellular polarity suggests a further maturation step following implantation (Figures 4C–4E).

Transplantation of Human nSPHs in Mouse CKD Models

Having shown the *in vivo* differentiation potential of nSPH-derived cells, we were next interested in testing their therapeutic potential. For this purpose, we used the 5/6 nephrectomy mouse CKD model (Harari-Steinberg et al., 2013). In this model, NOD/SCID mice first undergo resection of two-thirds of a kidney, and 1 week later, the contralateral kidney is resected, thereby removing 5/6 of total renal mass. After 2 weeks, blood and 24 h urine are collected and used to assess pre-treatment blood creatinine (Cr) levels and Cr clearance (CrCl). Initially, we tested whether injected nSPH-derived cells could survive and integrate into the remnant kidney. On the basis of the data outlined above, we transplanted 7–8 d cultured nSPH-derived cells. Analysis of human nSPHs directly implanted into the remnant mouse kidney 48 h and 2 weeks following implantation showed cell engraftment, as indicated by HLA staining (Figure 5A). Moreover, the cells were seen to generate engrafted renal structures (Figure 5A). Thus, the tubulogenic potential demonstrated by the s.c. transplantation assay was recapitulated in host diseased kidneys without the support of Matrigel. The engraftment ability of human nSPH comprised cell survival, proliferation, organization, and differentiation processes, suggesting that the nSPHs might be able to exert an *in vivo* therapeutic potential. In order to assess such a potential therapeutic effect, 80 mice were treated with either 1.5–2 × 10^6 nSPH-derived cells (n = 43) or saline (n = 37), administered via intra-parenchymal injections into the remnant kidney, at three separate time points (4, 7, and 10 weeks following the initial resection; see Figure 5B). To evaluate kidney function following treatment, blood and 24 h urine samples were collected 2 weeks after the first injection, 2 weeks after the second injection, and 2, 5, and 8 weeks following the third and last injection (Figure 5B). Finally, following the last collection of blood and urine, the mice were sacrificed and their remnant kidneys removed for histological analysis. Relative changes (percentages) in blood Cr and calculated CrCl from pre-injection to each post-injection time point are shown in Tables S4 and S5. Analysis of nSPH-treated mice showed a significant decrease in blood Cr and an increase in CrCl after the second injection compared with pre-injection (Cr, $p = 0.032$; CrCl, $p = 0.045$; Figures 5C and 5D). Similarly, in the nSPH group, blood Cr showed a significant reduction and CrCl a significant elevation after the third injection compared with pre-injection at all time points analyzed (3i: Cr, $p < 0.0001$; CrCl, $p = 0.0014$; 3ii: Cr, $p = 0.0013$; CrCl, $p = 0.041$; 3iii: Cr, $p < 0.0001$; CrCl, $p = 0.009$; mean of all post-third injection measurements: Cr, $p < 0.0001$; CrCl, $p = 0.0002$) (Figures 5C and 5D; Tables S4 and S5, upper panel). Interestingly, we observed that although the murine model generates excessively abnormal blood Cr and CrCl levels, and severe renal disease was attained throughout the 18 week experimental protocol, some level of spontaneous improvement of kidney function appeared also in the saline group with time, albeit statistically significant only at the post-third injection time point compared with pre-injection (Figures 5C and 5D; Tables S4 and S5, upper panel). Subsequently, to gain a comprehensive understanding of the efficacy of the treatment, we applied the mixed-effect model for repeated measures (MMRM), in which blood Cr levels and CrCl from all post-injection time points are integrated and compared with pre-treatment levels. Remarkably, using MMRM adjusted to donor, the reduction in blood Cr and increase in CrCl from pre-injection were significantly greater in the nSPH group compared with the saline group ($p = 0.0288$ and $p = 0.034$, respectively) (Tables S4 and S5, lower panel). These data are in line with very recent publications that identify changes in renal function between treatment groups over time, as an endpoint in randomized controlled trials in CKD (Inker et al., 2019; Grams et al., 2019). Furthermore, analysis of changes in Cr and CrCl between treatment groups showed that the reduction in blood Cr from pre-injection to after the third injection (mean of all time points) was significantly greater in the nSPH group (23.6% ± 18.3%) than in the saline group (13.8% ± 23.0%) ($p = 0.048$ adjusted to donor) (Figure 5E). Similarly, the increase in CrCl from pre-injection to after the third injection (mean of all time points) was greater in the nSPH group (102.4% ± 136.2%) than in the saline group (53.6% ± 94.8%) ($p = 0.052$ adjusted to donor) (Figure 5F). Analysis of 24 h urine protein (Upr) showed increased levels in both nSPH-treated mice and the saline group, but no significant changes were observed between groups, and proteinuria of increasing severity was not apparent in nSPH-treated mice as renal function improved (MMRM, $p = 0.88$; change in Upr after the third injection, $p = 0.69$). Having observed a beneficial therapeutic effect of nSPH in the remnant kidney injury model, we tested nSPH cell transplantation in an additional model. In this

(B) nSPHs survive and massively generate structures when injected for 2 and 5 weeks, as indicated by HLA staining (green). Scale bars, 200 μm.
(C) nSPH morphology at day 3 (left) and day 7 (right) in non-adherent conditions. Scale bars, 100 μm.
(D) Structures generated from day 3 (left) and day 7 (right) nSPHs, 2 weeks following s.c. injection into mice. Scale bars, 50 μm.
(E) The difference in the number of structures between day 3 and day 7 nSPHs. Scale bars, 20 μm.
(F) nSPH-derived tubules, stained for HLA.
(G) 3D projection from confocal images of whole grafts stained for HLA (Alexa 488, green) and Hoechst (blue).
See also Video S1. Scale bars, 25 μm.

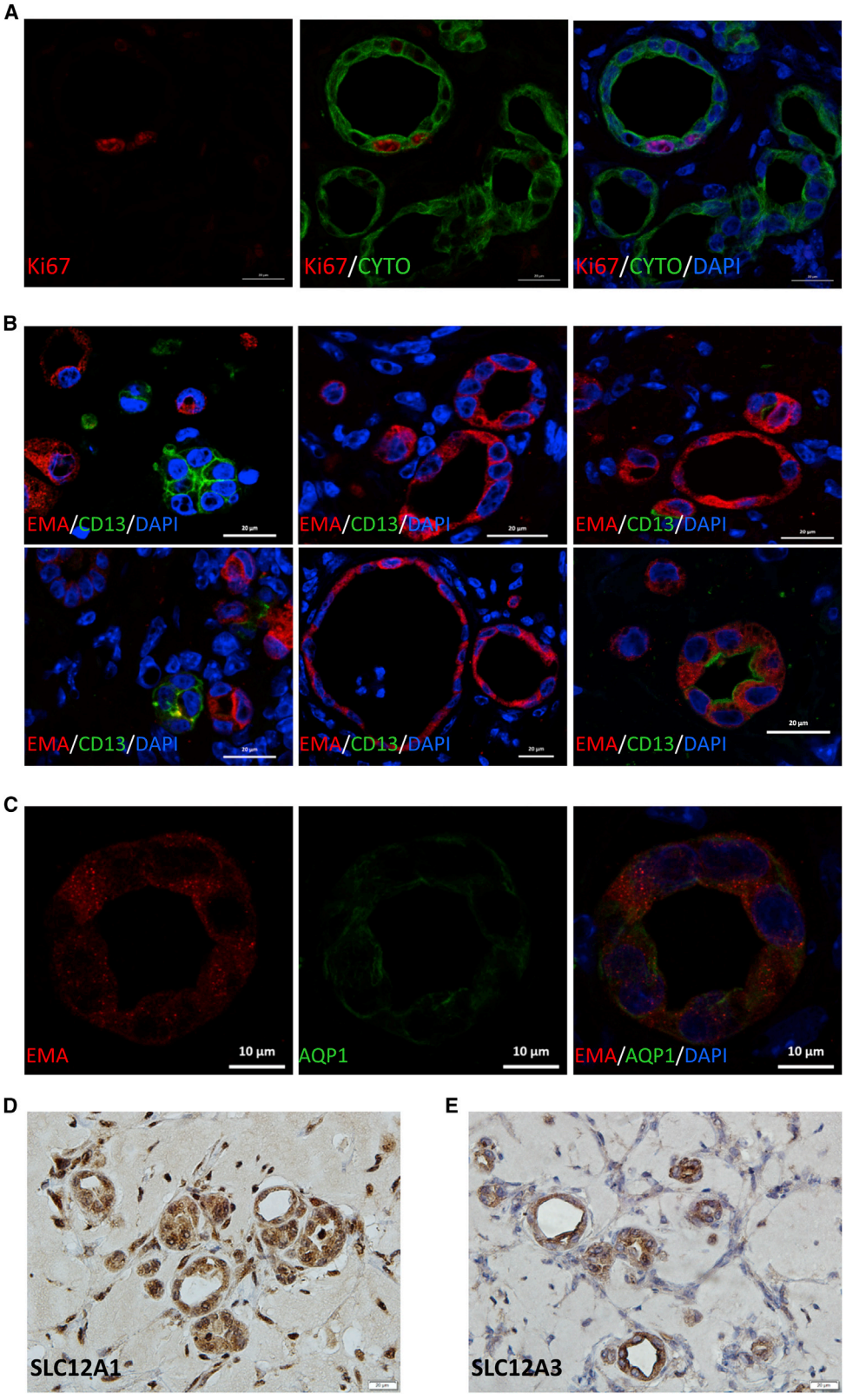

(legend on next page)

model we used cisplatin (CP) injections on days 0 and 14 to induce kidney injury (Safirstein et al., 1986), followed by unilateral nephrectomy (UNx) to generate a more advanced CKD (Figure S4A). One million to two million nSPH-derived cells were directly administered 2 weeks after UNx into the contralateral kidney. We analyzed the long-term effects of nSPH by measuring changes in blood Cr (compared with those measured after UNx) 4 weeks after cell grafting. Accordingly, treated mice showed a significantly blunted Cr elevation (Figure S4B). Thus, human nSPHs induce a beneficial effect on kidney function in chronic renal injury models.

To further determine the mechanism underlying the functional improvement, we carried out histological analysis of the kidneys. HLA staining of the kidneys demonstrated robust engraftment of nSPHs in the remnant kidney (Figure 6A). Because human nSPHs were administered at 4, 7, and 10 weeks (see scheme in Figure 5B), these results indicate survival of cells for at least 8 weeks and up to 14 weeks. Long-term engraftment of the cells in the kidney consisted mostly of self-organizing human tubular structures (Figure 6B) or cell condensates composed of a small number of cells (Figures 6C and 6D). In addition, single-cell engraftment was observed within host mouse tubules (Figures 6E and 6F) and rarely in the tubulo-interstitial space (Figure 6G). A similar long-term engraftment pattern was noted in the CP+UNx model (Figure S4C). Thus, cell-cell interaction of donor epithelial cells in engrafted structures promotes long-term survival in disease microenvironment. Finally, using confocal microscopy and HLA staining for human donor cells, we queried donor-host tubular interactions in the remnant kidney, detecting possible sites of connection between the tubular systems (Figures 6H–6P; Figure S4D).

Derivation of Functional nSPHs from Non-functional Human Kidneys

Having established that nSPH-derived cells isolated from healthy kidneys have regenerative capacity, we next asked whether nSPHs with similar potential can be derived from CKD and ESRD patients, as this would mean that nSPHs could potentially serve as an autologous renal cell therapy. Toward this aim, we attempted to isolate and characterize cells from nephrectomies of diseased and ESRD non-functional kidneys (NFKs). Patient characteristics (n = 15) are presented in Table S6, and representative H&E and CD13/EMA stainings of patient kidney sections are shown in Figure S5A. Two-dimensional hKEpC cultures, as well as 3D nSPHs thereof, were successfully generated from all NFKs. Notably, the yield of generating hKEpCs was similar in functional kidneys (FK-hKEpCs) and NFKs (NFK-hKEpC) at P0 (Figure S5B). In addition, doubling time values of FK-hKEpCs and NFK-hKEpC were similar (approximately 90, 42, and 46 h at passages 1, 2, and 3, respectively). NFK-hKEpCs in P1–P3 invariably demonstrated the ability to grow in 3D conditions and generate NFK-nSPHs (Figure S5C). Flow cytometry analysis and immunostaining showed NFK-hKEpCs and NFK-nSPHs to harbor similar characteristics to FK-hKEpCs and FK-nSPHs (Figures S5D–S5F). Thus, our *in vitro* culture conditions allowed establishment of 2D hKEpCs and 3D nSPHs with the same attributes regardless of the functional state of the kidneys from which they were derived. Next, using RNA-seq, we compared the entire transcriptome of NFK-nSPHs with that of FK-nSPHs. Importantly, to maximize the translational relevance of the experiment, we used human serum at the 2D hKEpC expansion stage. Temporal transcriptional analysis of NFK-nSPHs at 3, 6, and 9 days showed similar processes to be taking place as in FK-nSPHs, including activation of renal developmental genes, epithelial differentiation, and acquisition of renal identity, reduced cell cycle and EMT (Figure 7A; Figures S6A–S6D). Specifically, a volcano plot analysis of the transcriptomes of FK-nSPHs and NFK-nSPHs pinpointed concomitant significantly overexpressed proximal-specific > distal region-specific markers (SLC22A6 [OAT1], LRP2, AQP1, SLC12A1, KCNJ1, CASR, and SLC24A3) and the epithelial transcription factors (TFs) (HNF4A and GRHL2) (Figure S6E). Finally, we sought to determine the *in vivo* potential of NFK-nSPHs using the s.c. transplantation assay in NOD/SCID mice (see above), by assessing their tubulogenic potential at 2 and 5 weeks after implantation (Figure 7B). The tubulogenic potential of NFK-nSPHs, as well as their ability to proliferate, were retained in the kidney environment following renal subcapsular transplantation, as evident by the nuclear Ki-67 staining (Figure 7C). Moreover, transplantation of NFK-nSPHs into long-standing remnant kidneys (12–15 weeks after the second contralateral nephrectomy) showed engraftment of human renal structures at 2 weeks as indicated by HLA staining. CD13/EMA staining disclosed proximal and distal tubular identity (Figures 7D and 7E). Single-cell engraftment of human cells into mouse tubules was also observed showing chimeric tubules with individual human EMA+ and CD13+ cell engraftment (Figure 7E). Thus, the *in vivo* potential of NFK-nSPHs to generate engrafted renal structures or integrate into existing structures is similar to that of FK-nSPHs. As an extreme example, we further highlight tissue collected from the native kidney of a patient who received a renal allograft 15 years ago. The patient recently underwent nephrectomy of his native end-stage kidney, which enabled us to test the capacity of functional nSPH derivation from an almost entirely scarred kidney residing for many years in the body as a non-functioning organ (Figure S6F). In order to achieve a useful cell amount in this clinical scenario, proliferative hKEpCs were expanded for two more passages (Figure S6G) before generating nSPHs. Strikingly, the s.c. grafting assay revealed nSPH to generate renal structures (Figures S6H and S6I), while the corresponding hKEpCs completely

Figure 4. nSPH Generate Renal Tubular Epithelial Structures of Different Nephron Segments

(A) Tubule-like structures generated from nSPHs were stained for Ki-67 and cytokeratin, demonstrating epithelial structures harboring cells that are actively proliferating following engraftment. Scale bars, 20 μm.

(B) Engrafted structures were stained for the proximal and distal tubule markers CD13 and EMA, respectively. We detected structures harboring a single phenotype (distal/proximal, top row), as well as a mixed phenotype (bottom row). Scale bars, 20 μm.

(C–E) Engrafted structures were positively stained for transporter markers: AQP1 (proximal tubule), scale bars, 10 μm. (C), SLC12a1 (loop of Henle) (D), and SLC12a3 (distal tubule) (E). Scale bars, 20 μm.

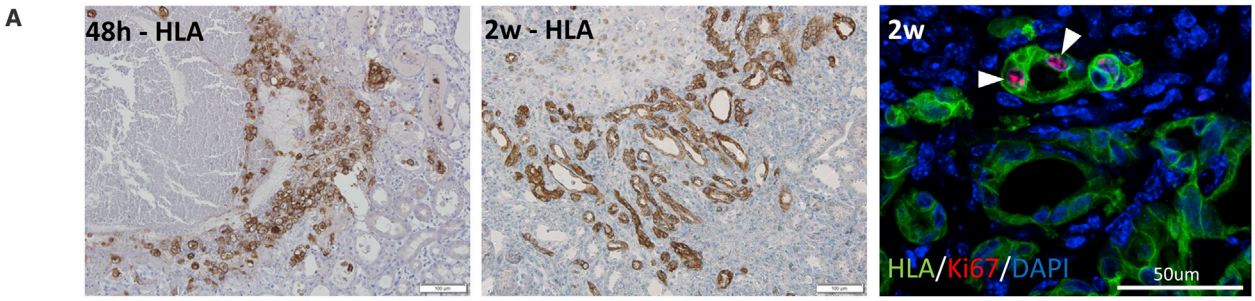

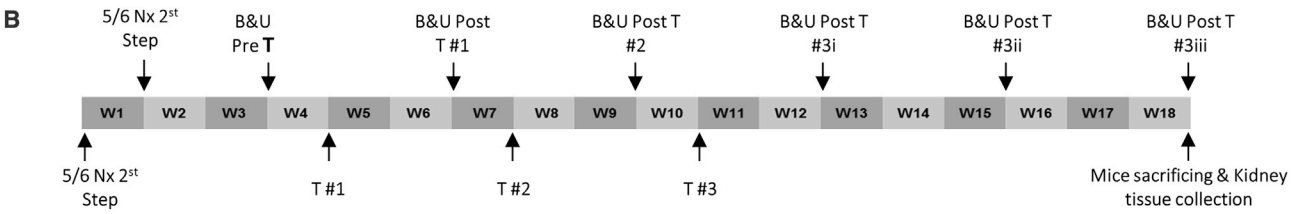

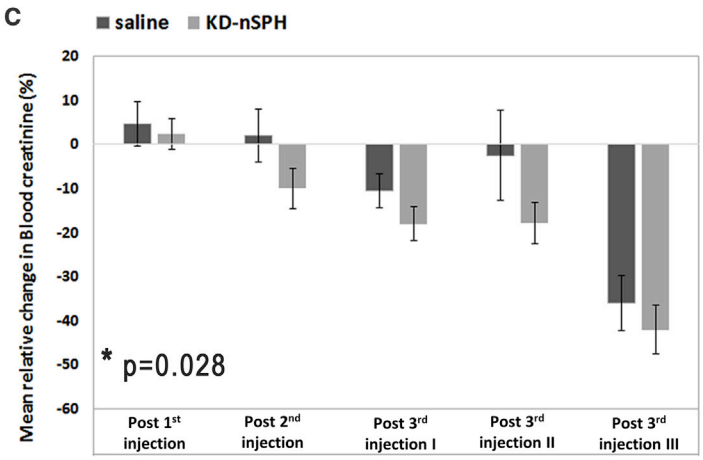

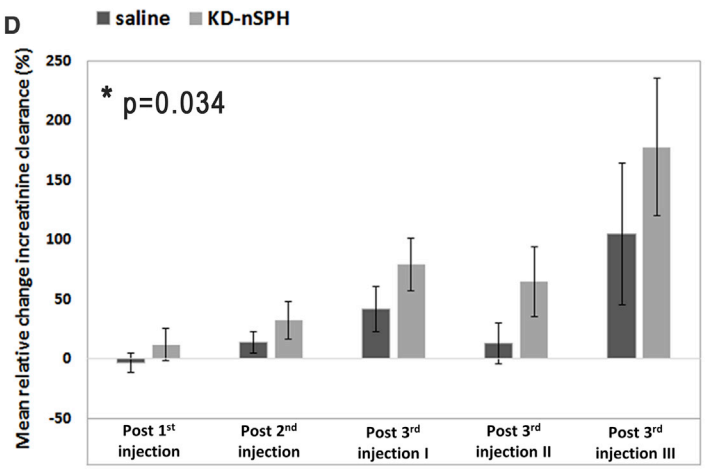

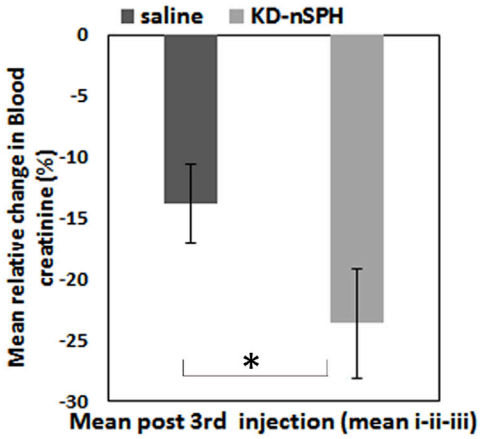

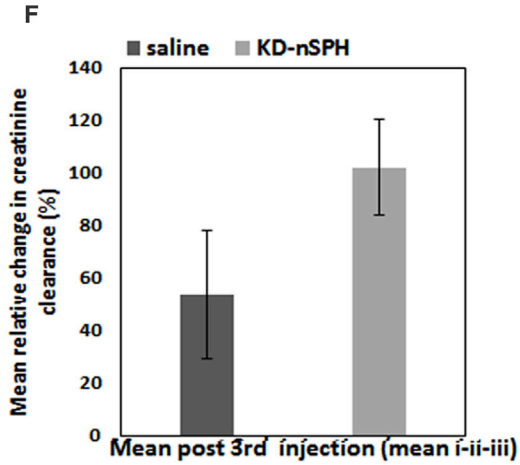

(legend on next page)

failed to do so, showing mere survival post-transplantation (Figure S6H).

Altogether, our protocol for nSPH derivation from the adult kidney enriches for the same type of cells independent of the clinical specimen obtained, indicating the relevance of NFK-nSPH for autologous renal cell therapy.

nSPHs Exert an Anti-fibrogenic and Regenerative Effect

To further interrogate the mechanism of action of nSPHs, we specifically queried the expression of stress-induced tubular epithelia-derived molecules that mediate kidney fibrosis in nSPHs derived from both FKs and NFKs. CTGF (Rayego-Mateos et al., 2018), DKK3 (Federico et al., 2016), COL1A1 (Glick et al., 1992), SNAI1 (Simon-Tillaux and Hertig, 2017), LOX (Di Donato et al., 1997; Goto et al., 2005), LOXL2 (Cosgrove et al., 2018), IL6 (Su et al., 2017), and TGFBI (Romagnani et al., 2015; Wing et al., 2014) were all significantly decreased in both FK-nSPHs and NFK-nSPHs (Figure S7A). Similarly, the senescence-associated secretory phenotype (SASP) of CKD (Valentijn et al., 2018) was dampened in nSPH (Figure S7B). In addition, suppressed fatty acid (FA) oxidation has been recently suggested as a mechanism for kidney epithelial fibrotic injury in CKD (Stadler et al., 2015; Li et al., 2009; Tran et al., 2011; Chou et al., 2017). Remarkably, analysis of FA oxidation pathway molecules showed upregulation in nSPH (of which BBOX1, an enzyme responsible for L-carnitine biosynthesis and critical for FA influx and tubular mitochondrial function [Vaz and Wanders, 2002], was mostly elevated; Figure S7C). These data, as well as combined GSEA enriching plots of EMT and fibrosis, FA oxidation, and the GLIS2 mouse (a genetic mouse model of progressive tubular atrophy and fibrosis leading to terminal CKD), support the notion that renal epithelia are revitalized in 3D nSPH cultures, even when derived from end-stage kidneys (Figure S7D). Moreover, transcriptional profiling of secreted-type molecules that are significantly overexpressed across FK-nSPH and NFK-nSPH samples and may mediate an active anti-fibrotic/anti-inflammatory mechanism disclosed anti-fibrotic DKK1 (Ren et al., 2013), FGL2, a well-established anti-inflammatory molecule (Chan et al., 2003; Zheng et al., 2007; Williams and Rudensky, 2007), APOE, the LRP2/megalin ligand, and Klotho, shown to harbor a renoprotective role (Chen et al., 2001; Zou et al., 2018) (Figure S7E). Having observed this signature of nSPHs, we next analyzed whether they can induce anti-fibrotic effects, using co-culture experiments in which NFK-nSPHs were placed in proximity to fibroblasts, but not allowing direct contact (Figure 7F). NFK-nSPHs actively inhibited the production of fibrosis-related genes, in fibroblasts, including collagen molecules (COL1A2, COL3A1, and COL4A1) indicating a paracrine mechanism of action (Figure 7G). In addition, nSPHs inhibited the expression of a series of inflammatory molecules related to collagen production in co-cultured fibroblasts, most notably STAT6, which has recently been put forward as harboring a major role in kidney fibrosis (Liang et al., 2017; Yan et al., 2015) (Figure S7F). Modulation of STAT6 levels by addition of IL-13 partially inhibited the effects of nSPH on collagen expression (loss of significant inhibition of COL1A2 expression but not of COL3A1), suggesting that nSPHs exploit STAT6, at least in part, to mediate a paracrine anti-fibrotic effect. Importantly, similar co-culture experiments using MSCs and fibroblasts showed no effect on collagen expression or STAT6 levels, suggesting a paracrine advantage for nSPH (Figure S7G).

Finally, to gain additional insight into the effects of donor nSPHs on host tissue, we performed RNA-seq of remnant and CP-UNx mouse kidneys 1 week after nSPH implantation by comparison with untreated controls (n = 3). The human transcriptome can be discriminated from the mouse counterpart, and therefore specific changes in the mouse can be queried. To determine enriched pathways in nSPH-treated kidneys in an unbiased manner, we applied Ingenuity pathway analysis (IPA). The most significantly activated pathway was mitotic roles of Polo-Like Kinase ($p = 10^{-12}$), while the most significantly inhibited pathway was G2/M DNA damage checkpoint regulation ($p = 10^{-7}$), altogether indicating release from the G2/M checkpoint and progression into mitosis (Figure S8A), which was evident in both disease models. Interestingly, G2/M arrest of tubular cells at this checkpoint is an important process of CKD progression (Canaud et al., 2019; Yang et al., 2010). Having observed these gene modules to globally differentially express, we further specifically analyzed the expression of PRC1, which was among the most significantly upregulated mouse gene transcripts in nSPH-treated kidneys. Importantly, inhibited PRC1 induces G2/M phase arrest and blocks mitotic exit, leading in turn to

Figure 5. Engraftment of nSPH Improves Kidney Function in the 5/6 Nephrectomy CKD Model

(A) Analysis of human nSPHs directly implanted into the remnant mouse kidney after 48 h and 2 weeks. Left and middle panels: immunohistochemistry (IHC) staining for HLA. Right panel: confocal microscopy image of double staining for HLA (green) and Ki-67 (red), demonstrating that engrafted structures harbor proliferating cells. DAPI, blue. Scale bars: left and middle panels, 100 μm; right panel, 50 μm.

(B) Experimental scheme. First, NOD/SCID mice underwent a two-step nephrectomy (Nx) procedure, in which two-thirds of one kidney, and 1 week later the entire contralateral kidney, were resected, thereby removing 5/6 of total renal mass. Two weeks later, blood (B) and urine (U) samples were collected to assess pre-treatment blood creatinine levels and creatinine clearance (CrCl). Eighty mice were randomly assigned for treatment with either nSPHs (n = 43) or saline (n = 37), via intra-parenchymal injections into the remnant kidney, at three time points (T1, T2, and T3). Blood and urine were collected 2 weeks after T1 (post-T1), 2 weeks after T2 (post-T2), and 2, 5, and 8 weeks following T3 (post-T3i, post-T3ii, and post-T3iii, respectively). Then, the mice were sacrificed, and the remnant kidney was removed for histological analysis.

(C) Relative change (percentage) in blood creatinine in the treatment (nSPH) and control (saline) groups, at each of the five measurements, compared with pre-treatment levels ($p = 0.028$, mixed model of repeated-measures).

(D) Relative change (percentage) in CrCl in the nSPH and saline groups, at each of the five measurements, compared with pre-treatment levels ($p = 0.034$, mixed model of repeated-measures).

(E) Relative change (percentage) in blood creatinine in the treatment (nSPH) and control (saline) groups, at the post-third injection stage (mean of all time points), compared with pre-treatment levels ($p = 0.048$, t test).

(F) Relative change (percentage) in CrCl in the treatment (nSPH) and control (saline) groups, at the post-third injection stage (mean of all time points), compared with pre-treatment levels ($p = 0.052$, t test). Error bars represent the mean ± SE.

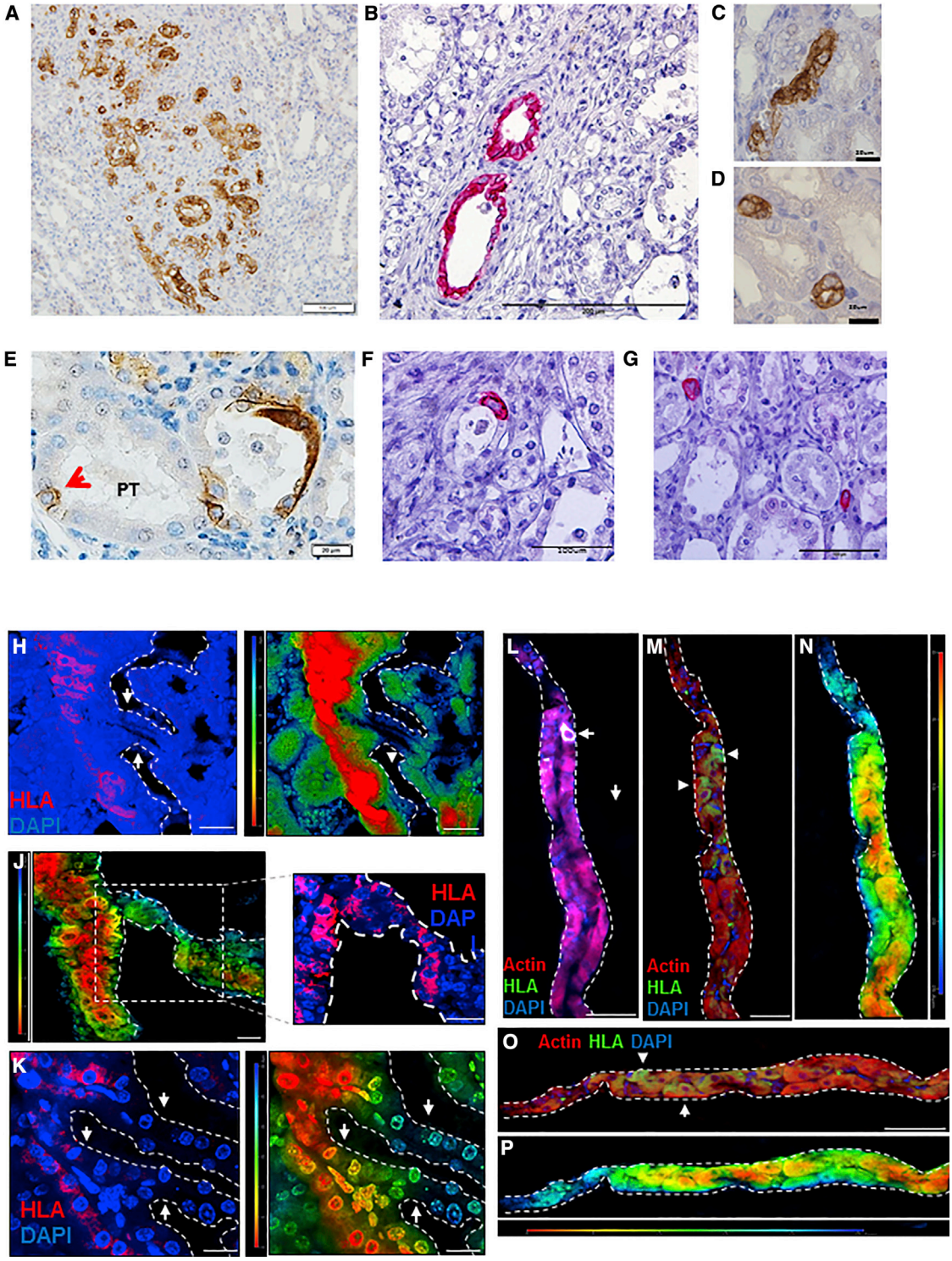

Figure 6. Patterns of nSPH Engraftment in the Remnant Kidney

(A–D) After 18 weeks of experimental protocol, remnant kidneys were removed and stained for the human-specific marker HLA (AP, pink; HRP, brown; light microscopy). Long-term engraftment (at least 2 months; see scheme in Figure 5B) consists of nSPH-derived tubular structures. (A) Low magnification, demonstrating the formation of numerous tubular structures. (B) Self-organizing human tubular structures. (C and D) Cell condensates. Scale bars: (A) 100 μm; (B) 200 μm; (C and D) 20 μm.

(E–G) Less frequent engraftment patterns include engraftment and integration of donor nSPH cells into existing host mouse tubules (E, red arrow, and F) and rare single cells between host tubules (G). Scale bars: (E) 20 μm; (F and G) 100 μm.

(legend continued on next page)

apoptosis and cell death (Li et al., 2004; Zhan et al., 2017). We stained PRC1 in the remnant (5/6) and CP-UNx mouse kidneys 1 month after nSPH transplantation to assess long-term effects. Analysis of nuclear PRC1 protein expression showed significantly elevated levels in treated mouse kidneys, specifically in host mouse tubules, potentially indicating a reduction in G2/M arrest and progression to mitosis allowing an endogenous reparative response in host diseased kidneys (Figures S8B–S8D).

DISCUSSION

In this study, we show the relevance of *ex vivo* cultured 3D nSPHs derived from the human adult kidney as cell therapy for the failing kidney. Human nSPHs engraft in mouse kidneys, give rise to renal parenchyma, and halt the progression of CKD in mice. Thus, adult kidney-derived nSPHs are a unique source of transplantable progenitors for renal cellular therapies. Moreover, nSPHs can be readily obtained from biopsies of a collection of diseased or non-functional human kidneys, a process that will enable autologous use and offer the advantage of rapid translation to a clinically established procedure.

Using next-generation sequencing, we revealed that although human adult kidney expanded in adherent cultures upregulates hundreds of proliferation-related, cell-cycle, and EMT genes, genes involved in kidney epithelial cell function are repressed. In contrast, when generating human nSPHs, a process of "rebuilding the kidney" takes place in primary cultures so that developmental pathways of MET and renal epithelialization are activated, and tissue-specific genes of various nephron segments are temporally upregulated, reverting from de-differentiated to differentiating renal epithelia. These changes of cellular de-differentiation and re-differentiation have a profound functional consequence; s.c. human/mouse grafting experiments in NOD/SCID mice show nSPHs to harbor enhanced intrinsic renal potency in an adult mouse environment. Although the culture of proliferative 2D hKEpCs is crucial for expansion, cells are already de-differentiated at P1 to the extent that upon s.c. grafting, acquisition of epithelial phenotype is limited. Thus, the ability to form tubuloids *in vivo* is a unique feature of nSPH-derived single cells, one shared by P0 proliferative hKEpCs but that is significantly lost later on. Strikingly, in all our hKEpC, nSPH, and NFK-nSPH human/mouse grafting experiments into s.c. or Matrigel, renal capsule, and remnant kidney, engraftment at 2 weeks and above is observed mostly as self-organizing epithelial condensates and 3D tubular organoids, while individual cells that are not in physical interaction with other cells are only seldom retained with time. This engraftment pattern is most notable when grafting the cells into chronically diseased mouse kidneys (remnant and CP/UNx). Thus, a mechanism of donor cells to avoid elimination and long-term survive *in vivo* in a hostile environment is via self-organization into structures, a characteristic akin to 3D nSPHs. Major obstacles of cellular-based therapies are the low engraftment and poor survival of transplanted cells in the harmful microenvironment of the host, severely limiting cells' functional attributes to a short time window. Accordingly, strategies allowing cell retention in the transplanted area are of the utmost importance, especially in chronic progressive disease, which imposes extreme conditions on donor cells (Madonna et al., 2019; Moriarty et al., 2019; Squires et al., 2017). In that regard, our data drawing a line between *in vitro* 3D epithelial cell cultures that harbor organogenic properties to *in vivo* long-term engraftment and survival of transplanted cells afford a conceptual advance to the cell therapy field and may be of relevance to remodeling of other chronically injured epithelial organs.

Beneficial effects on changes in blood Cr levels and glomerular filtration rate (GFR), determinants of renal function, accompanied *in vivo*, long-term engraftment that followed nSPH transplantation in chronic kidney injury models (remnant; CP/UNx), showing a prolonged effect. Moreover, improved renal function in the remnant model was not accompanied by progressively increased urinary protein levels, which remained like controls. This is of importance because an unwanted trade-off may exist in progressive and advanced CKD between improved renal function and consequent elevated proteinuria, which is in turn independently detrimental to future renal function (Turin et al., 2013; Iseki, 2013). In the remnant model, a need for multiple transplantations along disease progression was required to attain a functional benefit. An ongoing injury process that affects the initial inoculum of cells engrafting and integrating in the diseased kidney may account for the need for additional cycles of cell therapy. These data corroborate recent publications in clinical cell therapy of various fields which indicate that single cell transfers have little impact on efficacy and suggest that repeated cell transfers are necessary (Bolli, 2017). Thus, the need for repeated cell therapy is likely to be crucial to future

(H–K) Grafted human nSPH cells can form connections with mouse renal architecture. (H) Confocal 3D rendered z stack shadow image of kidney tissue immunostained with anti-HLA antibody to mark grafted human cells. Cell nuclei are counterstained using DAPI. Dotted white lines demarcate connection of grafted cells to the mouse renal architecture. A depth-coded image of (H) is shown in (I). Depth-coded 3D rendered z stack of kidney tissue (J) demonstrates same level surface connection (green). Inset shows zoom-in on connected region displaying HLA+ grafted human cells. Cell nuclei were counterstained using DAPI. Immunostained and depth-coded images (K) demonstrate a clear connection between grafted and mouse renal cells. Dashed lines demarcate borders and arrows indicate architectural connection.

(L) Confocal image of kidney tissue immunostained with anti-HLA antibody and phalloidin (actin) to mark grafted human cells. Cell nuclei are counterstained using DAPI. Dotted white lines demarcate mouse renal architecture.

(M) Confocal 3D rendered z stack image of kidney tissue immunostained with anti-HLA antibody and phalloidin (actin) to mark grafted human cells. Cell nuclei are counterstained using DAPI. Dotted white lines demarcate renal architecture.

(N) Depth-coded image of (M).

(O) Confocal 3D rendered z stack side view image of kidney tissue immunostained with anti-HLA antibody and phalloidin (actin) to mark grafted human cells. Cell nuclei are counterstained using DAPI.

(P) Depth- coded image of (O).

Scale bars, 50 μm (H, I, L, M, and O) and 20 μm (J and K).

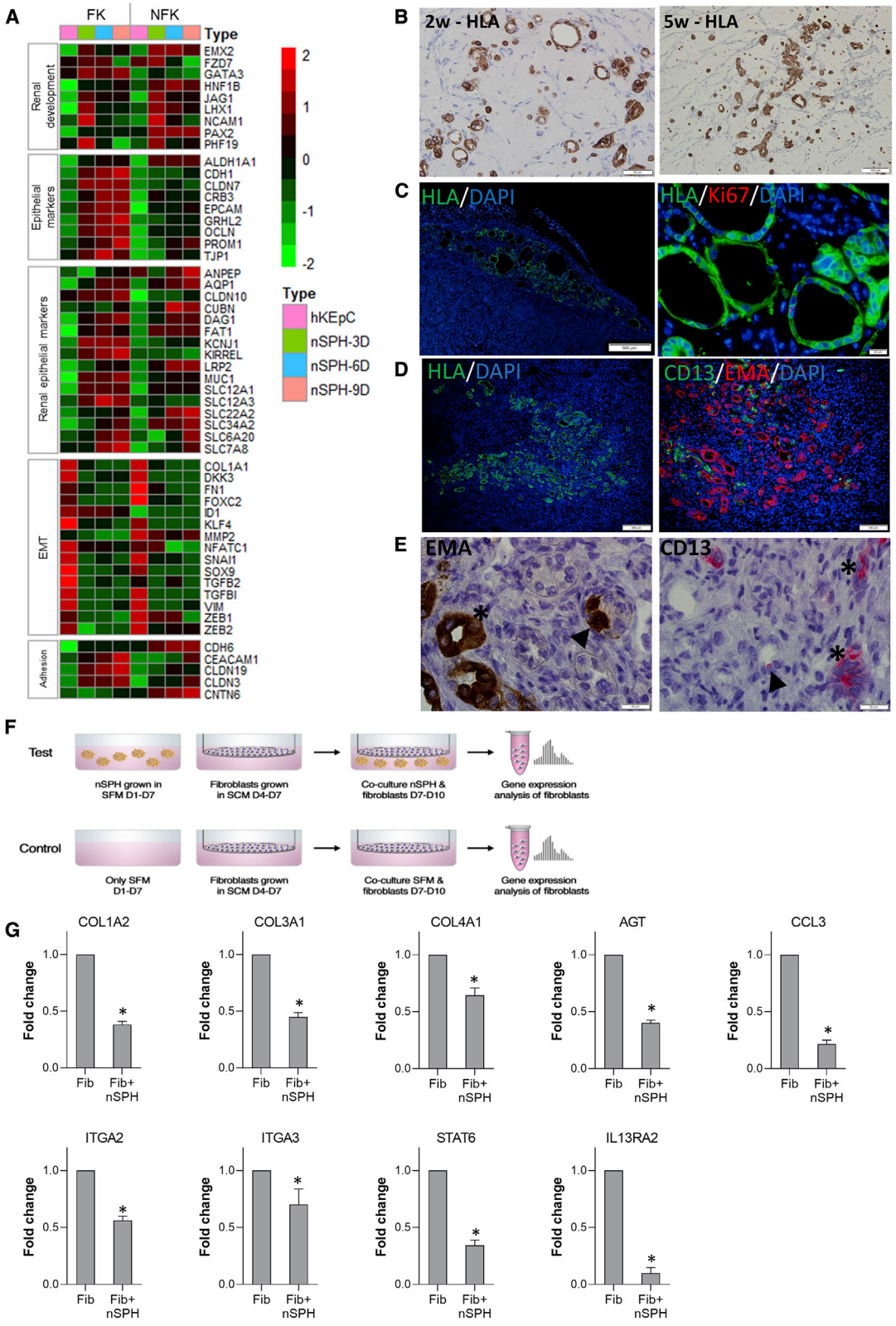

(legend on next page)

clinical protocol development. The use of a single cell harvest in such a protocol is advantageous. In this regard, the ability to obtain non-functioning human CKD tissue and to restore renal epithelia *ex vivo* is critical. Indeed, the surprising capacity to derive proliferative hKEpCs and establish nSPHs from unique clinical samples of end-stage kidneys that match healthy counterparts supports the derivation of autologous nSPH with regenerative potential from CKD patients toward the establishment of a clinical procedure from a single harvest. In addition, these data may extend beyond cell therapy and into the realm of kidney bioengineering in which the rescued autologous renal parenchyma from ''useless'' end-stage kidneys is combined with kidney scaffold, obviating the utilization of an autologous iPS-based protocol (Shafiee and Atala, 2017, Morizane et al., 2017).

The progression of CKD is characterized by the loss of renal cells and nephron subunits and their replacement by extracellular matrix (ECM), irrespective of the originating disease (Nogueira et al., 2017). In addition, renal tubular epithelia become pro-fibrotic, senescent, and arrested in cell cycle, losing endogenous repair and regenerative mechanisms (Rinkevich et al., 2014; Valentijn et al., 2018). It is noteworthy that human renal epithelial cells recapitulate a more natural microenvironment in 3D nSPHs, manifested by shutdown of pro-fibrotic/inflammatory genes and activation of FA oxidation, and as shown resemble the mirror image of stressed CKD epithelia, thus potentially providing revitalized donor cells irrespective of the mechanism of repair. In that regard, nSPHs may intervene by various modes to achieve a therapeutic benefit; in our current transplantation model, single-cell replacement appears to be limited. In contrast, nSPH-derived cells self-organize to form spheres and tubuloids (within the interstitium) that are retained long term after transplantation, allowing prolonged and continuous donor-host interaction (Figure 6). These interactions include possible inter-species tubule connections leading to the addition of nephron subunits (Figures 6H–6K) and/or cross-talk with ECM and host epithelia via paracrine routes (Figure 7). Further studies are needed to understand the relative contribution of each mechanism. Herein, we queried the paracrine route in detail; renal fibroblasts play a key role in CKD, leading to excessive matrix deposition and a perpetuation of pro-fibrotic signaling. Using a co-culture model, we showed paracrine inhibitory effects of nSPHs on collagen and inflammatory molecule synthesis. More specifically, we show inhibition of STAT6/IL13R2 in fibroblasts and that activation of STAT6 partially reverted the effects of nSPHs on collagen synthesis (COL1A1), indicating yet additional mechanisms of action. Nevertheless, because STAT6 is a major pro-fibrotic signal in kidney fibrocytes, future studies delivering nSPHs and pharmacologic inhibition of STAT6 may induce synergistic effects. Other secreted-type anti-fibrotic/inflammatory and renal-protective molecules that are constantly elevated in nSPHs, such as DKK1/FLG2/Klotho, may be tested alongside nSPHs. Strikingly, MSCs, previously suggested as a reservoir of regenerative molecules working in a paracrine manner, did not inhibit collagen synthesis or STAT6 levels. Thus, nSPH cell therapy for CKD may be unique in targeting fibroblast behavior in a paracrine fashion. Finally, we assessed donor-host interactions by specifically analyzing mouse kidney transcriptome 1 week after nSPH transplantation into diseased mouse kidneys. Unbiased pathway analysis uncovered combined inhibition of G2/M checkpoint regulation and activation of mitotic PLK1, as the two most altered modules suggesting increased signatures of proliferation and a release from the quiescent state. Remarkably, PRC1 (the most upregulated transcript alongside FAM83D), whose knockdown has been shown to induce a G2/M phase arrest (Zhan et al., 2017), showed enhanced nuclear staining specifically localized to host tubular epithelia 1 month after nSPH transplantation, indicative of a long-standing effect. Thus, donor nSPHs may activate endogenous cells long term, with renal repair capacity that is lost in CKD, affording therapeutic benefit.

STAR★METHODS

Detailed methods are provided in the online version of this paper and include the following:

- KEY RESOURCES TABLE
- LEAD CONTACT AND MATERIALS AVAILABILITY
- EXPERIMENTAL MODEL AND SUBJECT DETAILS
  - Establishment of primary cultures from human kidney
  - nSPH formation and dismantling
  - Animal experiments
- METHOD DETAILS
  - RNA sequencing
  - Sequence alignment and analysis

Figure 7. Profile upon Generating 3D nSPHs and Anti-fibrotic Effects of nSPHs

(A and B) Heatmap representation of differentially expressed genes in FK and NFK cultures, showing the similarity in gene expression between FK- and NFK-hKEpCs and nSPHs (A). In both FK-nSPHs and NFK-nSPHs, renal developmental genes are initially upregulated (day 3) and then downregulated (days 6–9), there is robust activation of epithelial-related pathways (i.e., upregulation of kidney epithelial genes and downregulation of EMT-related genes), and cell-cell adhesion molecules are upregulated (B) structures *in vivo* and integrate into host tubules. Immunostaining for HLA of NFK-nSPH-derived cells that were subcutaneously injected into NOD-SCID mice, for 2 or 5 weeks. NFK-nSPHs generate tubule-like structures. Scale bars: left panel, 50 μm; right panel, 100 μm.

(C) Tubulogenic potential was retained in the renal environment, as shown by staining for HLA and Ki-67, of renal subcapsular-transplanted NFK-nSPHs. Scale bars: left panel, 500 μm; right panel, 20 μm.

(D and E) Transplantation of NFK-nSPHs into long-standing remnant kidneys, visualized 2 weeks post-injection. (D) Left panel: staining for HLA. Right panel: double staining for the proximal and distal tubule markers CD13 and EMA, respectively. Scale bars: left panel, 200 μm; right panel, 100 μm. (E) Staining for EMA (left panel) and CD13 (right panel), showing tubules expressing EMA and tubules expressing CD13 (asterisk). In addition, single-cell engraftment of donor human cells into mouse tubules showing chimeric tubules with individual human EMA+ or CD13+ cells residing in mouse tubules (black arrowheads) was also observed. Scale bars: 20 μm.

(F) Scheme of co-culture fibrosis assay model (see also STAR Methods).

(G) qPCR analysis of fibroblasts grown with NFK-nSPHs derived from three donors (Fib+nSPH) or without NFK-nSPH (Fib) for collagens and inflammatory related molecules ($p < 0.05$, all levels). Error bars represent the mean ± SE.

- Heat-maps, barplots, and PCA
- GSEA analysis
- Gene Clustering and Enrichment Analysis
- Agarose block preparation
- Immunofluorescence staining (IF)
- Immunohistochemical (IHC) staining
- Flow cytometry
- Grafting Cells in NOD/SCID Mice (tubule formation assay)
- Whole Matrigel graft staining and imaging
- 5/6-Nephrectomy model of chronic renal disease in NOD-SCID mice
- Cisplatin/ unilateral nephrectomy disease model
- Fibrosis assay
- Efficacy experiments

● QUANTIFICATION AND STATISTICAL ANALYSIS
- Tubular quantification
- PRC1 quantification

● DATA AND CODE AVAILABILITY

SUPPLEMENTAL INFORMATION

Supplemental Information can be found online at https://doi.org/10.1016/j.celrep.2019.12.047.

ACKNOWLEDGMENTS

We wish to thank the entire staff at the Pediatric Stem Cell Research Institute at the Sheba Medical Center for the fruitful discussions. We wish to thank Dr. Tali Bar-Lev from the Faculty of Engineering and Bar-Ilan Institute of Nanotechnology and Advanced Materials (BINA) at Bar-Ilan University for assistance with the bioinformatic experiments, Michael Namestnikov for assistance with generating the summarizing scheme, and the Israel National Center for Personalized Medicine (INCMP) for their assistance in sequencing and analysis. This study was supported by KidneyCure Bio and the Sheba Medical Center (B.D.) and the Israel Science Foundation (ICORE 1902/12 and grants 1634/13 and 2017/13), the Israel Ministry of Health (grant 3-10146), and the European Union (EU) Seventh Framework Programme (FP7) (Marie Curie International Reintegration grant 618592) (T.K.).

AUTHOR CONTRIBUTIONS

Experiment Design, O.H.-S., D.O., and B.D.; Experiment Performance, D.O., Y.G., S.G., O.C.-Z., S.P.-C., Y.F., and Z.D.; Data Analysis and Manuscript Writing, O.H.-S., D.O., O.P., and B.D.; RNA Quality Checks for Sequencing, I.K., and T.K.; RNA-Seq Data Preprocessing and Analysis, O.H.S, O.C.-Z., I.K., N.B.H., E.B., and T.K.

DECLARATION OF INTERESTS

B.D is a co-founder, shareholder, and board member at KidneyCure. O.H.S is a shareholder at KidneyCure.

Received: January 6, 2019
Revised: October 4, 2019
Accepted: December 12, 2019
Published: January 21, 2020

REFERENCES

Anders, S., McCarthy, D.J., Chen, Y., Okoniewski, M., Smyth, G.K., Huber, W., and Robinson, M.D. (2013). Count-based differential expression analysis of RNA sequencing data using R and Bioconductor. Nat. Protoc. *8*, 1765–1786.

Anders, S., Pyl, P.T., and Huber, W. (2015). HTSeq—a Python framework to work with high-throughput sequencing data. Bioinformatics *31*, 166–169.

Bolli, R. (2017). Repeated cell therapy: a paradigm shift whose time has come. Circ. Res. *120*, 1072–1074.

Buzhor, E., Harari-Steinberg, O., Omer, D., Metsuyanim, S., Jacob-Hirsch, J., Noiman, T., Dotan, Z., Goldstein, R.S., and Dekel, B. (2011). Kidney spheroids recapitulate tubular organoids leading to enhanced tubulogenic potency of human kidney-derived cells. Tissue Eng. Part A *17*, 2305–2319.

Canaud, G., Brooks, C.R., Kishi, S., Taguchi, K., Nishimura, K., Magassa, S., Scott, A., Hsiao, L.L., Ichimura, T., Terzi, F., et al. (2019). Cyclin G1 and TASCC regulate kidney epithelial cell G_2-M arrest and fibrotic maladaptive repair. Sci. Transl. Med. *11*, eaav4754.

Chan, C.W., Kay, L.S., Khadaroo, R.G., Chan, M.W., Lakatoo, S., Young, K.J., Zhang, L., Gorczynski, R.M., Cattral, M., Rotstein, O., and Levy, G.A. (2003). Soluble fibrinogen-like protein 2/fibroleukin exhibits immunosuppressive properties: suppressing T cell proliferation and inhibiting maturation of bone marrow-derived dendritic cells. J. Immunol. *170*, 4036–4044.

Chen, G., Paka, L., Kako, Y., Singhal, P., Duan, W., and Pillarisetti, S. (2001). A protective role for kidney apolipoprotein E. Regulation of mesangial cell proliferation and matrix expansion. J. Biol. Chem. *276*, 49142–49147.

Chen, J., Bardes, E.E., Aronow, B.J., and Jegga, A.G. (2009). ToppGene Suite for gene list enrichment analysis and candidate gene prioritization. Nucleic Acids Res. *37*, W305–W311.

Chou, H.C., Wen, L.L., Chang, C.C., Lin, C.Y., Jin, L., and Juan, S.H. (2017). From the cover: l-carnitine via PPARγ- and Sirt1-dependent mechanisms attenuates epithelial-mesenchymal transition and renal fibrosis caused by perfluorooctanesulfonate. Toxicol. Sci. *160*, 217–229.

Cosgrove, D., Dufek, B., Meehan, D.T., Delimont, D., Hartnett, M., Samuelson, G., Gratton, M.A., Phillips, G., MacKenna, D.A., and Bain, G. (2018). Lysyl oxidase like-2 contributes to renal fibrosis in Col4α3/Alport mice. Kidney Int. *94*, 303–314.

Di Donato, A., Ghiggeri, G.M., Di Duca, M., Jivotenko, E., Acinni, R., Campolo, J., Ginevri, F., and Gusmano, R. (1997). Lysyl oxidase expression and collagen cross-linking during chronic adriamycin nephropathy. Nephron *76*, 192–200.

Dziedzic, K., Pleniceanu, O., and Dekel, B. (2014). Kidney stem cells in development, regeneration and cancer. Semin. Cell Dev. Biol. *36*, 57–65.

Federico, G., Meister, M., Mathow, D., Heine, G.H., Moldenhauer, G., Popovic, Z.V., Nordström, V., Kopp-Schneider, A., Hielscher, T., Nelson, P.J., et al. (2016). Tubular Dickkopf-3 promotes the development of renal atrophy and fibrosis. JCI Insight *1*, e84916.

Freedman, et al. (2015). Nat Commun.

Glick, A.D., Jacobson, H.R., and Haralson, M.A. (1992). Mesangial deposition of type I collagen in human glomerulosclerosis. Hum. Pathol. *23*, 1373–1379.

Goto, Y., Uchio-Yamada, K., Anan, S., Yamamoto, Y., Ogura, A., and Manabe, N. (2005). Transforming growth factor-beta1 mediated up-regulation of lysyl oxidase in the kidneys of hereditary nephrotic mouse with chronic renal fibrosis. Virchows Arch. *447*, 859–868.

Grams, M.E., Sang, Y., Ballew, S.H., Matsushita, K., Astor, B.C., Carrero, J.J., Chang, A.R., Inker, L.A., Kenealy, T., Kovesdy, C.P., et al. (2019). Evaluating glomerular filtration rate slope as a surrogate end point for ESKD in clinical trials: an individual participant meta-analysis of observational data. J. Am. Soc. Nephrol. *30*, 1746–1755.

Harari-Steinberg, O., Metsuyanim, S., Omer, D., Gnatek, Y., Gershon, R., Pri-Chen, S., Ozdemir, D.D., Lerenthal, Y., Noiman, T., Ben-Hur, H., et al. (2013). Identification of human nephron progenitors capable of generation of kidney structures and functional repair of chronic renal disease. EMBO Mol. Med. *5*, 1556–1568.

Inker, L.A., Heerspink, H.J.L., Tighiouart, H., Levey, A.S., Coresh, J., Gansevoort, R.T., Simon, A.L., Ying, J., Beck, G.J., Wanner, C., et al. (2019). GFR slope as a surrogate end point for kidney disease progression in clinical trials: a meta-analysis of treatment effects of randomized controlled trials. J. Am. Soc. Nephrol. *30*, 1735–1745.

Iseki, K. (2013). Chronic kidney disease: proteinuria as a predictor of rapid eGFR decline. Nat. Rev. Nephrol. *9*, 570–571.

Kim, D., Pertea, G., Trapnell, C., Pimentel, H., Kelley, R., and Salzberg, S.L. (2013). TopHat2: accurate alignment of transcriptomes in the presence of insertions, deletions and gene fusions. Genome Biol. *14*, R36.

Kobayashi, A., Valerius, M.T., Mugford, J.W., Carroll, T.J., Self, M., Oliver, G., and McMahon, A.P. (2008). Six2 defines and regulates a multipotent self-renewing nephron progenitor population throughout mammalian kidney development. Cell Stem Cell *3*, 169–181.

Li, C., Lin, M., and Liu, J. (2004). Identification of PRC1 as the p53 target gene uncovers a novel function of p53 in the regulation of cytokinesis. Oncogene *23*, 9336–9347.

Li, S., Nagothu, K.K., Desai, V., Lee, T., Branham, W., Moland, C., Megyesi, J.K., Crew, M.D., and Portilla, D. (2009). Transgenic expression of proximal tubule peroxisome proliferator-activated receptor-alpha in mice confers protection during acute kidney injury. Kidney Int. *76*, 1049–1062.

Liang, H., Zhang, Z., Yan, J., Wang, Y., Hu, Z., Mitch, W.E., and Wang, Y. (2017). The IL-4 receptor α has a critical role in bone marrow-derived fibroblast activation and renal fibrosis. Kidney Int. *92*, 1433–1443.

Little, M., Georgas, K., Pennisi, D., and Wilkinson, L. (2010). Kidney development: two tales of tubulogenesis. Curr. Top. Dev. Biol. *90*, 193–229.

Little, M.H., Combes, A.N., and Takasato, M. (2016). Understanding kidney morphogenesis to guide renal tissue regeneration. Nat. Rev. Nephrol. *12*, 624–635.

Liyanage, T., Ninomiya, T., Jha, V., Neal, B., Patrice, H.M., Okpechi, I., Zhao, M.H., Lv, J., Garg, A.X., Knight, J., et al. (2015). Worldwide access to treatment for end-stage kidney disease: a systematic review. Lancet *385*, 1975–1982.

Love, M.I., Huber, W., and Anders, S. (2014). Moderated estimation of fold change and dispersion for RNA-seq data with DESeq2. Genome Biol. *15*, 550.

Madonna, R., Van Laake, L.W., Botker, H.E., Davidson, S.M., De Caterina, R., Engel, F.B., Eschenhagen, T., Fernandez-Aviles, F., Hausenloy, D.J., Hulot, J.S., et al. (2019). ESC Working Group on Cellular Biology of the Heart: position paper for Cardiovascular Research: tissue engineering strategies combined with cell therapies for cardiac repair in ischaemic heart disease and heart failure. Cardiovasc. Res. *115*, 488–500.

Magella, B., Adam, M., Potter, A.S., Venkatasubramanian, M., Chetal, K., Hay, S.B., Salomonis, N., and Potter, S.S. (2018). Cross-platform single cell analysis of kidney development shows stromal cells express Gdnf. Dev. Biol. *434*, 36–47.

Metsuyanim, S., Pode-Shakked, N., Schmidt-Ott, K.M., Keshet, G., Rechavi, G., Blumental, D., and Dekel, B. (2008). Accumulation of malignant renal stem cells is associated with epigenetic changes in normal renal progenitor genes. Stem Cells *26*, 1808–1817.

Moriarty, N., Parish, C.L., and Dowd, E. (2019). Primary tissue for cellular brain repair in Parkinson's disease: promise, problems and the potential of biomaterials. Eur. J. Neurosci. *49*, 472–486.

Morizane, R., Miyoshi, T., and Bonventre, J.V. (2017). Concise review: kidney generation with human pluripotent stem cells. Stem Cells *35*, 2209–2217.

National Institute of Diabetes and Digestive and Kidney Diseases (2016). Kidney Disease Statistics for the United States.https://www.niddk.nih.gov/health-information/health-statistics/kidney-disease.

Nogueira, A., Pires, M.J., and Oliveira, P.A. (2017). Pathophysiological mechanisms of renal fibrosis: a review of animal models and therapeutic strategies. In Vivo *31*, 1–22.

Noiman, T., Buzhor, E., Metsuyanim, S., Harari-Steinberg, O., Morgenshtern, C., Dekel, B., and Goldstein, R.S. (2011). A rapid in vivo assay system for analyzing the organogenetic capacity of human kidney cells. Organogenesis *7*, 140–144.

Pleniceanu, O., Harari-Steinberg, O., and Dekel, B. (2010). Concise review: kidney stem/progenitor cells: differentiate, sort out, or reprogram? Stem Cells *28*, 1649–1660.

Pleniceanu, O., Omer, D., Harari-Steinberg, O., and Dekel, B. (2018). Renal lineage cells as a source for renal regeneration. Pediatr. Res. *83*, 267–274.

Pode-Shakked, N., Pleniceanu, O., Gershon, R., Shukrun, R., Kanter, I., Bucris, E., Pode-Shakked, B., Tam, G., Tam, H., Caspi, R., et al. (2016). Dissecting stages of human kidney development and tumorigenesis with surface markers affords simple prospective purification of nephron stem cells. Sci. Rep. *6*, 23562.

Pode-Shakked, N., Gershon, R., Tam, G., Omer, D., Gnatek, Y., Kanter, I., Oriel, S., Katz, G., Harari-Steinberg, O., Kalisky, T., and Dekel, B. (2017). Evidence of in vitro preservation of human nephrogenesis at the single-cell level. Stem Cell Reports *9*, 279–291.

Rayego-Mateos, S., Morgado-Pascual, J.L., Rodrigues-Diez, R.R., Rodrigues-Diez, R., Falke, L.L., Mezzano, S., Ortiz, A., Egido, J., Goldschmeding, R., and Ruiz-Ortega, M. (2018). Connective tissue growth factor induces renal fibrosis via epidermal growth factor receptor activation. J. Pathol. *244*, 227–241.

Ren, S., Johnson, B.G., Kida, Y., Ip, C., Davidson, K.C., Lin, S.L., Kobayashi, A., Lang, R.A., Hadjantonakis, A.K., Moon, R.T., and Duffield, J.S. (2013). LRP-6 is a coreceptor for multiple fibrogenic signaling pathways in pericytes and myofibroblasts that are inhibited by DKK-1. Proc. Natl. Acad. Sci. U S A *110*, 1440–1445.

Rinkevich, Y., Montoro, D.T., Contreras-Trujillo, H., Harari-Steinberg, O., Newman, A.M., Tsai, J.M., Lim, X., Van-Amerongen, R., Bowman, A., Januszyk, M., et al. (2014). In vivo clonal analysis reveals lineage-restricted progenitor characteristics in mammalian kidney development, maintenance, and regeneration. Cell Rep. *7*, 1270–1283.

Romagnani, P., Rinkevich, Y., and Dekel, B. (2015). The use of lineage tracing to study kidney injury and regeneration. Nat. Rev. Nephrol. *11*, 420–431.

Safirstein, R., Winston, J., Goldstein, M., Moel, D., Dikman, S., and Guttenplan, J. (1986). Cisplatin nephrotoxicity. Am. J. Kidney Dis. *8*, 356–367.

Shafiee, A., and Atala, A. (2017). Tissue engineering: toward a new era of medicine. Annu. Rev. Med. *68*, 29–40.

Simon-Tillaux, N., and Hertig, A. (2017). Snail and kidney fibrosis. Nephrol. Dial. Transplant. *32*, 224–233.

Squires, J.E., Soltys, K.A., McKiernan, P., Squires, R.H., Strom, S.C., Fox, I.J., and Soto-Gutierrez, A. (2017). Clinical hepatocyte transplantation: what is next? Curr. Transplant. Rep. *4*, 280–289.

Stadler, K., Goldberg, I.J., and Susztak, K. (2015). The evolving understanding of the contribution of lipid metabolism to diabetic kidney disease. Curr. Diab. Rep. *15*, 40.

Su, H., Lei, C.T., and Zhang, C. (2017). Interleukin-6 signaling pathway and its role in kidney disease: an update. Front. Immunol. *8*, 405.

Subramanian, A., Tamayo, P., Mootha, V.K., Mukherjee, S., Ebert, B.L., Gillette, M.A., Paulovich, A., Pomeroy, S.L., Golub, T.R., Lander, E.S., and Mesirov, J.P. (2005). Gene set enrichment analysis: a knowledge-based approach for interpreting genome-wide expression profiles. Proc. Natl. Acad. Sci. U S A *102*, 15545–15550.

Taguchi, et al. (2017). Cell Stem Cell.

Tran, M., Tam, D., Bardia, A., Bhasin, M., Rowe, G.C., Kher, A., Zsengeller, Z.K., Akhavan-Sharif, M.R., Khankin, E.V., Saintgeniez, M., et al. (2011). PGC-1α promotes recovery after acute kidney injury during systemic inflammation in mice. J. Clin. Invest. *121*, 4003–4014.

Turin, T.C., James, M., Ravani, P., Tonelli, M., Manns, B.J., Quinn, R., Jun, M., Klarenbach, S., and Hemmelgarn, B.R. (2013). Proteinuria and rate of change in kidney function in a community-based population. J. Am. Soc. Nephrol. *24*, 1661–1667.

Valentijn, F.A., Falke, L.L., Nguyen, T.Q., and Goldschmeding, R. (2018). Cellular senescence in the aging and diseased kidney. J. Cell Commun. Signal. *12*, 69–82.

Vaz, F.M., and Wanders, R.J. (2002). Carnitine biosynthesis in mammals. Biochem. J. *361*, 417–429.

Williams, L.M., and Rudensky, A.Y. (2007). Maintenance of the Foxp3-dependent developmental program in mature regulatory T cells requires continued expression of Foxp3. Nat. Immunol. *8*, 277–284.

Wing, M.R., Devaney, J.M., Joffe, M.M., Xie, D., Feldman, H.I., Dominic, E.A., Guzman, N.J., Ramezani, A., Susztak, K., Herman, J.G., et al.; Chronic Renal Insufficiency Cohort (CRIC) Study (2014). DNA methylation profile associated with rapid decline in kidney function: findings from the CRIC study. Nephrol. Dial. Transplant. *29*, 864–872.

Yan, J., Zhang, Z., Yang, J., Mitch, W.E., and Wang, Y. (2015). JAK3/STAT6 stimulates bone marrow-derived fibroblast activation in renal fibrosis. J. Am. Soc. Nephrol. *26*, 3060–3071.

Yang, L., Besschetnova, T.Y., Brooks, C.R., Shah, J.V., and Bonventre, J.V. (2010). Epithelial cell cycle arrest in G2/M mediates kidney fibrosis after injury. Nat. Med. *16*, 535–543.

Zhan, P., Zhang, B., Xi, G.M., Wu, Y., Liu, H.B., Liu, Y.F., Xu, W.J., Zhu, Q.Q., Cai, F., Zhou, Z.J., et al. (2017). PRC1 contributes to tumorigenesis of lung adenocarcinoma in association with the Wnt/β-catenin signaling pathway. Mol. Cancer *16*, 108.

Zheng, Y., Josefowicz, S.Z., Kas, A., Chu, T.T., Gavin, M.A., and Rudensky, A.Y. (2007). Genome-wide analysis of Foxp3 target genes in developing and mature regulatory T cells. Nature *445*, 936–940.

Zou, D., Wu, W., He, Y., Ma, S., and Gao, J. (2018). The role of klotho in chronic kidney disease. BMC Nephrol. *19*, 285.

STAR★METHODS

KEY RESOURCES TABLE

REAGENT or RESOURCE	SOURCE	IDENTIFIER
Antibodies		
Recombinant Rabbit Anti-HLA A antibody [EP1395Y]	abcam	Cat#ab52922; RRID:AB_881225
Mouse Anti-Human Ki67/MKI67 Clone MM1 mAb	Cell Sciences	Cat#MONX10283; RRID:AB_1833494
Rabbit anti-Cytokeratin, Wide Spectrum Screening	Dako	Cat#Z0622; RRID:AB_2650434
EMA (E29) Mouse Monoclonal Antibody	Cell Marque	Cat#247M-98; RRID:AB_1158303
Recombinant Anti-CD13 antibody [EPR4059]	abcam	Cat#ab108382; RRID:AB_10890797
Recombinant Rabbit Anti-Aquaporin 1 antibody [EPR11588(B)]	abcam	Cat#ab168387; RRID:AB_2810992
Rabbit anti-NKCC2/SLC12A1	NOVUS	Cat#NBP1-82559; RRID:AB_11031626
Rabbit anti-thiazide-sensitive NaCl cotransporter (NCC)/SLC12A3	Merck	Cat#AB3553; RRID:AB_303900
Rabbit Anti-PRC1 antibody [EP1513Y]	abcam	Cat#ab51248; RRID:AB_2284304
Alexa Fluor® 488 donkey anti mouse IgG	Invitrogen	Cat#A21202; RRID:AB_141607
Alexa Fluor® 555 donkey anti mouse IgG	Invitrogen	Cat#A31570; RRID:AB_2536180
ImmPRESS systems anti-mouse-HRP	Vector Laboratories	Cat#MP-7402; RRID:AB_2336528
ImmPRESS Anti-Rabbit Alkaline Phosphatase	Vector Laboratories	Cat#MP-5401; RRID:AB_2336536
Biological Samples		
Human kidney samples	Sheba medical center tissue bank	N/A
Chemicals, Peptides, and Recombinant Proteins		
Cisplatin	Sheba medical center pharmacy	N/A
Critical Commercial Assays		
Direct-zol RNA MiniPrep kit	ZYMO RESEARCH	Cat#R2050
OmniPrep solution (pH 9.0)	Zytomed Systems	Cat#ZUC067-500
Cas-Block solution	Invitrogen immunodetection	Cat#00-8120
ImmPACT DAB Peroxidase (HRP) Substrate kit	Vector Laboratories	Cat#SK-4105
Red Alkaline Phosphatase (Red AP) Substrate Kit	Vector Laboratories	Cat#SK-5100
Deposited Data		
RNA-seq data	NCBI GEO	GSE141257
Experimental Models: Organisms/Strains		
Mouse: male or female NOD-SCID	Envigo Israel	Cat#2N-SCID05
Software and Algorithms		
Gene Set Enrichment Analysis tool (GSEA)	GSEA	http://software.broadinstitute.org/gsea/index.jsp
R	The R Project for Statistical Computing	https://www.r-project.org/
TopHat2 v2.1.0	Johns Hopkins University	https://ccb.jhu.edu/software/tophat/index.shtml
FlowJo v7.6.5	Tree Star Inc. USA	https://www.flowjo.com/solutions/flowjo/
ImageJ/Fiji	ImageJ	https://imagej.net/Fiji/Downloads

LEAD CONTACT AND MATERIALS AVAILABILITY

Further information and requests for resources and reagents should be directed to and will be fulfilled by the lead contact, professor Benjamin Dekel (benjamin.dekel@gmail.com OR binyamin.dekel@sheba.health.gov.il).

No unique reagents were generated in this study.

EXPERIMENTAL MODEL AND SUBJECT DETAILS

Establishment of primary cultures from human kidney

Human kidney samples were retrieved from the borders of renal cell carcinoma (RCC) tumors resected from partial and total nephrectomy patients. Collected tissues were washed with PBS, weighed and minced into ~1 mm slices using sterile surgical scalpels. The dissected tissue was then incubated for two h at 37°C with Iscoves' Modified Dulbecco's Medium (IMDM) (Invitrogen) supplemented with 0.1% collagenase IV (Invitrogen). The digested tissue was sieved through 100 μm cell strainers to achieve a single cell suspension. The medium was removed by centrifugation and the cells were resuspended in growth medium and plated on gelatin-coated T175 flasks. Serum containing medium (SCM) was comprised of IMDM (Biological Industries) supplemented with 10% fetal bovine serum (Invitrogen), 1% Pen-strep 100M, 1% L-glutamine (both purchased from Biological industries), 100 ng/ml EGF, 100 ng/ml bFGF and 10 ng/ml SCF (all growth factors were purchased from Peprotech Asia). Cells were detached using 0.05% Trypsin/EDTA (Invitrogen) upon reaching confluency and cryopreserved in 10% DMSO FBS. 2D human kidney epithelial cells (hKEpC) were photographed using Nikon Eclipse TS100 and Nikon Digital Sight cameras.

nSPH formation and dismantling

hKEpC were thawed and grown as 2D monolayers for 5-7 days. Upon reaching confluency of 80%–100%, the cells were harvested and seeded on poly (2-hydroxyethylmethacrylate) (poly-HEMA; Sigma-Aldrich)-precoated plates, in serum free medium (SFM), at a concentration of 5.5–13x10^4 cells/mL. SFM was comprised of N2 medium (Biological Industries) supplemented with 1% Pen-strep 100M, 1% L-glutamine, 0.4% B27 supplement (GIBCO), 4μg/ml heparin sodium (Intramed), 1% non-essential amino acids, 1% sodium pyruvate, 0.2% CD Lipid concentrate (all purchased from Invitrogen), 2.4mg/ml glucose, 0.4mg/ml transferrin, 10mg/ml insulin, 38.66μg/ml putrescine, 0.04% sodium selenite, 12.6μg/ml progesterone (all from Sigma-Aldrich), 10ng/ml FGF and 20ng/ml EGF. nSPH were photographed using Nikon Eclipse TS100 and Nikon Digital Sight cameras. After 7-10 days in culture, nSPH were collected and dismantled by incubation with TrypLE (GIBCO) for 10 min. nSPH-derived cells were then counted for further experimentation. For generating agarose blocks and RNA, medium with two million nSPH cells was collected and centrifuged, and the nSPH pellet was retrieved.

Animal experiments

For the subcutaneous tubule formation assay, 7-8-weeks old male and female mice were used. For the 5/6 Nx experiments, 10-weeks old male and female NOD-SCID mice were used. For the cisplatin model experiments, 10-weeks old male and female NOD-SCID mice were used. In all experiments, mice were randomly assigned to treatment/control groups. This study was conducted according to the principles expressed in the Declaration of Helsinki. The study was approved by the Institutional Review Board of the Sheba Medical Center. Human kidney samples were retrieved from borders of renal cell carcinoma (RCC) tumors from partial and total nephrectomy patients, after obtaining informed consent and has been approved by the local ethical committee. All animal experiments were approved by the Committee for Ethics in Animal experimentation of the Sheba Medical Center, and Science in Action (SIA) animal facility.

METHOD DETAILS

RNA sequencing

Bulk total RNA was prepared from >10^5 cells that were isolated from nephrospheres using the Direct-zol RNA MiniPrep kit (Zymo Research) according to the manufacturer's instructions and stored in −80°C. RNA was quantified on an Agilent BioAnalyzer (Agilent Technologies) and aliquots of 500ng were used to generate cDNA libraries using the TruSeq mRNA-Seq library kit (Illumina). Libraries were sequenced 1 × 50 bases on the Illumina HiSeq 2000 platform.

Sequence alignment and analysis

Sequence data were analyzed using the protocol by Anders et al. (Anders et al., 2013, Bolli, 2017). Briefly, raw reads were aligned by TopHat2 (Kim et al., 2013) to the human hg19 genome. Aligned reads were counted by HTSeq (Anders et al., 2015). Data normalization and differential gene expression were done by DESeq2 (Love et al., 2014).

Heat-maps, barplots, and PCA

We generated heatmaps and barplots of selected genes marking specific lineages of the developing kidney according to the literature (Little et al., 2010). PCA analysis was performed on all genes. All analyses were done using MATLAB and R.

GSEA analysis

The Gene Set Enrichment Analysis tool (v 2.2.4) was used to find gene sets that were enriched in two gene lists ranked by correlation with CDH1 and FZD7 expression over 4 time points (hKEpC, Day 3, Day 6, Day 10) in a single sample (AK82). (Subramanian et al., 2005).

Gene Clustering and Enrichment Analysis

Normalized count files from each of the four nephrospheres (AK82, AK86, AK124, and AK125) were first filtered for lowly expressed genes, by removing genes whose average expression over all time points was below 30. We used K-means clustering (K = 16 for each individual nephrosphere) to find clusters of genes with similar expression profiles and extracted the mean expression profiles for each cluster. We performed gene enrichment analysis on each cluster of genes using ToppGene (Chen et al., 2009), and selected annotations related to kidney development, proliferation, structure, and function.

Agarose block preparation

Two million hKEpC and nSPH-derived cells were washed with PBS, fixed with 4% PFA for 2h, washed again with PBS and suspended in 200 μl of 2% UltraPure low melting point agarose (Invitrogen) (in 5% sucrose). Agarose with cells was then molded (the wide edge of 1 mL tip was cut and used as a mold), fixed with 4% PFA overnight and paraffin embedded.

Immunofluorescence staining (IF)

5 μM Paraffin sections were pre-treated with OmniPrep solution (pH 9.0) in 95°C for one h in accordance with the manufacturer's protocol (Zytomed Systems). Blocking was done using Cas-Block solution (Invitrogen immunodetection, 00-8120) for one h followed by one h incubation with two of the following primary antibodies: anti-HLA (Rb; 1/200; abcam, 52922), anti- Ki67 (MM1) (Ms; 1/100; Cellsciences; MONX10283), Anti-Cytokeratin (WSS) (Rb; 1/200; DAKO, Z0622), anti-EMA (Ms; 1/2 of the prediluted antibody; Cell Marque, 247M-98), anti-CD13 (Rb; 1/400; abcam, 108382), anti-CD31 (Rb; 1/100; abcam; 28364), anti-Aqp1 (Rb; 1/1000; abcam, 168387). Detection was done using alexa488 conjugated anti-rabbit and alexa555-conjugated anti-mouse secondary antibodies (Invitrogen) for 60 min. Mounting medium containing DAPI (Dapi Fluoromount-G; SouthernBiotech, 0100-20) was applied. Slides were analyzed using Olympus BX51 fluorescent microscope and Olympus DP72 camera, or confocal microscope ZEISS LSM700. Photo analysis was done using ZEN software.

Immunohistochemical (IHC) staining

5 μM Paraffin sections were pre-treated using OmniPrep solution (pH 9.0) in 95°C for one h in accordance with the manufacturer's protocol (Zytomed Systems). Blocking was done using Cas-Block solution (Invitrogen immunodetection, 00-8120) for 20 min followed by incubation with one of the following primary antibodies: anti-HLA (Rb; 1/200; 1h; abcam, 52922), EMA (Ms; 1/4 of the prediluted antibody; 1h; Cell Marque, 247M-98), anti-CD13 (Rb; 1/400; 1h; abcam, 108382), anti-SLC12A1 (Rb; 1/1000, O.N; NOVUS, NBP1-82559), anti-SLC12A3 (Rb; 1/500, O.N; Merck, AB3553), anti-PRC1 (Rb; 1/100, 1h; abcam, 51248). Detection was done using one of Vector's ImmPRESS systems: anti-mouse-HRP (Vector, MP-7402) and anti-rabbit-HRP (Vector, MP-7401), both developed with DAB kit (Vector, SK-4105), or ImmPRESS Anti-Rabbit Alkaline Phosphatase (Vector, MP-5401) developed with Red Substrate Kit (Vector, SK-5100). All kits were used in accordance with the manufacturer's protocol. Hematoxylin was used for counterstaining.

Flow cytometry

$0.5X10^5$ cells were suspended in FACS buffer (0.5% BSA in 1X PBS). The cells were then incubated with a primary antibody or an isotype control (summarized above). Cell viability was tested using 7AAD viability staining solution (eBioscience). Cell labeling was detected using FACSCalibur (BD PharMingen). Flow cytometry results were analyzed using FlowJo analysis software (version 7.6.5).

Grafting Cells in NOD/SCID Mice (tubule formation assay)

In order to evaluate the cells' organization potential, two million hKEpC, nSPH-derived cells, fibroblasts (FIB) or mesenchymal stem cells (MSCs), were suspended in 200 μL Matrigel (MG) (BD Biosciences) and injected subcutaneously into NOD/SCID mice (Harlan Laboratories, Israel). At 14 days or five weeks after injection, the grafts were removed, paraffin-embedded, and sectioned for IF and IHC analyses.

Whole Matrigel graft staining and imaging

In order to evaluate the 3D nature of engrafted renal structures, we calibrated our HLA staining protocol for whole graft tissue instead of analyzing 5μM slices from paraffin embedded blocks. MG was fixed in 4% PFA overnight, washed with PBS and incubated in a shaker with Triton X-100 0.1% for 1.5h. MG was then incubated in a shaker for blocking overnight at 4°C, followed by incubation in a shaker with anti-HLA (Rb; 1/200; abcam, 52922) for 72 h at 4°C. Grafts were thoroughly washed with PBST (PBS + 0.05% Tween-20) and incubated in a shaker with a secondary antibody (alexa488 conjugated anti-rabbit; Invitrogen) for 1.5h. After thorough washing, the grafts were incubated in a shaker with Hoechst (33342) for 30 min, followed by PBST washes. Grafts were kept in mounting until imaging. Imaging was done using the Leica LSM confocal microscope.

5/6-Nephrectomy model of chronic renal disease in NOD-SCID mice

CKD was induced in NOD-SCID mice using the two-step 5/6 nephrectomy (Nx) model as previously described (Harari-Steinberg et al., 2013). This model was used to evaluate the therapeutic properties of the nSPH. One week after the second session, 1.5 – 2.5 million nSPH-derived cells were injected into the parenchyma of the remnant kidney in three separate injections at intervals of

three weeks between injections. 24-hour urine samples were collected two weeks after the second Nx stage and two weeks after each cell injection using metabolic cages. In addition, blood samples were collected from the retro-orbital sinus. After the last injection, two additional sampling points were added (three in total). For a scheme of the experiment layout see Figure 5B. 17 weeks after the second Nx session, the mice were sacrificed, and the kidneys were removed and paraffin embedded for IF and IHC analysis. CrCl in ml/min was calculated using the following formula: $\boldsymbol{CrCl = (U_{Cr} \times 24h\ volume)/(P_{Cr} \times 24 \times 60min).}$

Cisplatin/ unilateral nephrectomy disease model

10-week-old NOD-SCID mice were administered with two doses of 8mg/Kg cisplatin, at a two week interval. For the week following each administration the mice received IV hydration. 5 weeks following the second administration, one kidney was resected. Two weeks later, blood samples were retrieved from the retro-orbital sinus, in order to assess plasma creatinine. A week later, 2 million nSPH cells were injected into the remnant kidney. 5 weeks later, blood samples were collected. After another one week, the mice were sacrificed, and their kidneys were removed for histological analysis.

Fibrosis assay

nSPHs were co-cultured with human fibroblasts to determine a paracrine anti-fibrotic effect. hKEpC were seeded on polyhema-coated 6 well plates for nSPH formation and grown for 10 days. On day 7, human fibroblasts, grown on ThinCertsTM inserts (Greiner bio-one) for three days, were transferred to the nSPH wells for additional three days. On day 10, fibroblasts were harvested for RNA purification. Total RNA was prepared using Direct-zol RNA MiniPrep kit (Zymo Research) according to the manufacturer's instructions. Quantitative real-time PCR was carried out as previously described (Metsuyanim et al., 2008). TaqMan gene expression primers and probes were purchased from Thermo Fisher Scientific. For a scheme of the experiment see Figure 7F.

Efficacy experiments

Tables were provided giving sample size, arithmetic mean, standard deviation, minimum, median, maximum, and confidence interval for means of variables by treatment group. Paired-t tests were applied to determine the statistical significance of the relative changes (%) in blood creatinine and creatinine from pre-injection to each post-injection time point. Linear Regressions adjusted to donor were applied for testing the statistical significance of the difference between treatment groups in relative change in blood creatinine and creatinine clearance from pre-injection to post-3rd injection (the average of all time points post-3rd injection). Additional comparisons were applied using the MMRM model (Mixed-effect Model for Repeated-measures) adjusted to donor, with treatment groups as the between-subject factor and all the time-points as repeated-measurements. Comparisons were applied between the nSPH- and saline-treated groups in relative change in blood creatinine and creatinine clearance from pre-injection. All tests were two-tailed, and a p value of 5% or less was considered statistically significant. The data were analyzed using the SAS ® version 9.3 (SAS Institute, Cary North Carolina).

QUANTIFICATION AND STATISTICAL ANALYSIS

Error bars represent the mean ± SE, unless otherwise indicated. Statistical differences in gene expression (qPCR) and surface marker expression were evaluated using a non-paired 2-tailed t test. For all statistical analyses, the level of significance was set as $p < 0.05$. Sample size was chosen based on previous results of mean and standard deviation of blood Cr and CrCl in treated 5/6 Nx mice, requiring an alpha of 5%. All experiments were carried out in at least three biological replicates. The animals were randomized before cell injection for the treatment or control group. Data analysis was not blinded. Premature death was defined as a pre-determined exclusion criterion.

Tubular quantification

Three sections from each group were stained for HLA (IHC) and photos of ten fields were taken with an Olympus BX51 fluorescence microscope using Olympus DP72 camera at X40 magnification. The structures in each field were counted (see Figure S3E for a representative counting). The total number of structures from all fields was compared between the two groups.

PRC1 quantification

Three sections form each group were stained for PRC1 (IHC) and photos of ten fields were taken with an Olympus BX51 fluorescence microscope using Olympus DP72 camera at x40 magnification. The stained cells in each field were counted. The total number of stained cells from all fields was compared between the two groups.

DATA AND CODE AVAILABILITY

The RNA-seq data generated during this study are available at the Gene Expression Omnibus. The accession number for the RNA-seq data reported in this paper is GEO: GSE141257.

Cell Reports, Volume *30*

Supplemental Information

Ex Vivo Expanded 3D Human Kidney Spheres Engraft Long Term and Repair Chronic Renal Injury in Mice

Orit Harari-Steinberg, Dorit Omer, Yehudit Gnatek, Oren Pleniceanu, Sanja Goldberg, Osnat Cohen-Zontag, Sara Pri-Chen, Itamar Kanter, Nissim Ben Haim, Eli Becker, Roi Ankawa, Yaron Fuchs, Tomer Kalisky, Zohar Dotan, and Benjamin Dekel

Figure S1: Temporal GSEA analysis of SLCs, epithelialization and developmental pathways in nSPH (Related to Figure 1)

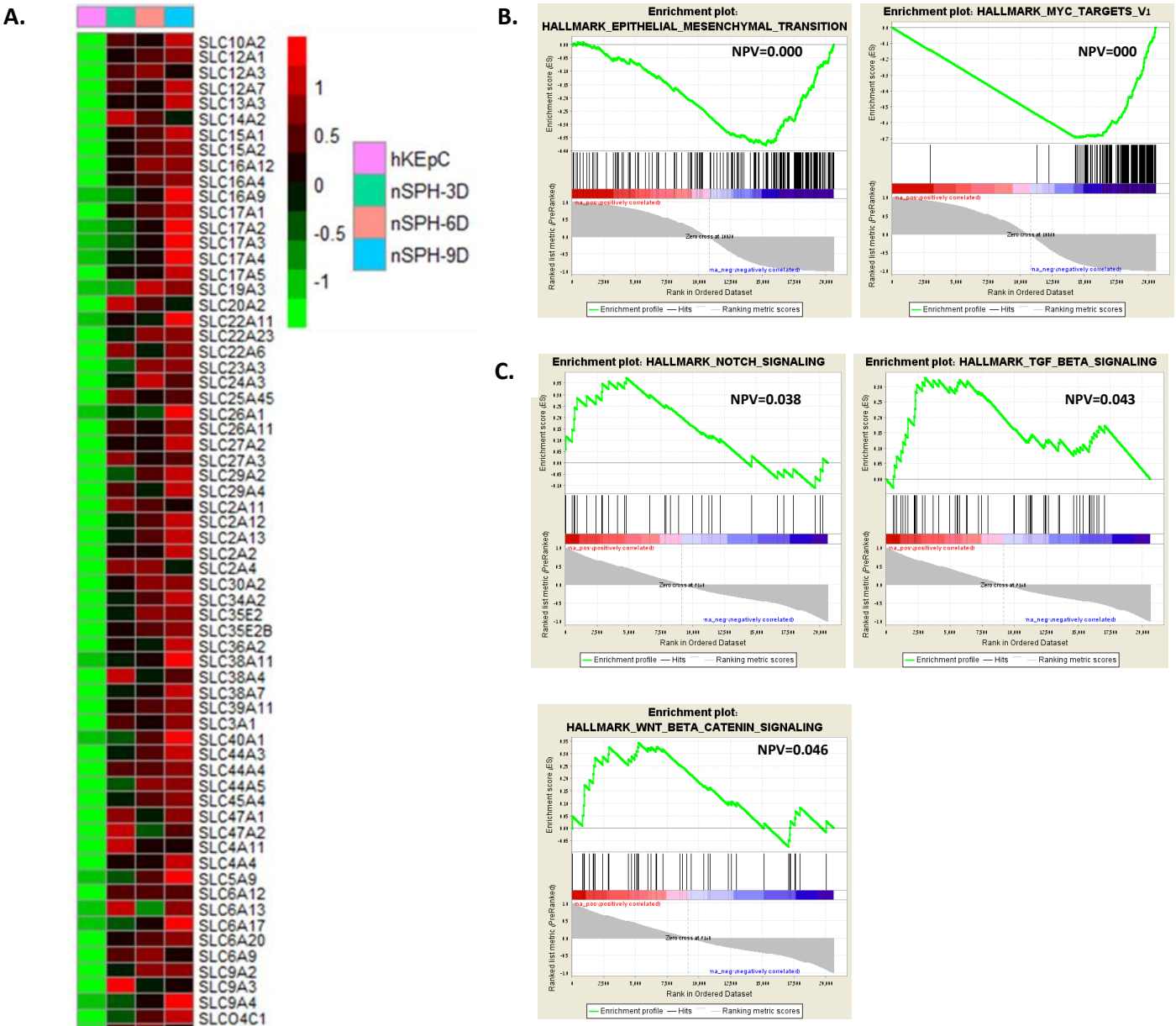

Figure S1: (A) Heatmap representation of solute carrier (SLC) genes up-regulated during nSPH formation (B) GSEA analysis of genes with similar expression pattern to *CDH1* uncovered down-regulation of the EMT and c-MYC pathways in nSPH. (C) GSEA analysis of genes with similar expression pattern to *FZD7* demonstrated early activation followed by down-regulation of developmental pathways (Notch, TGF-Beta, and Wnt) during nSPH formation.

Figure S2: CD13 and EMA represent proximal and distal markers in human adult and fetal kidneys (Related to Figure 2)

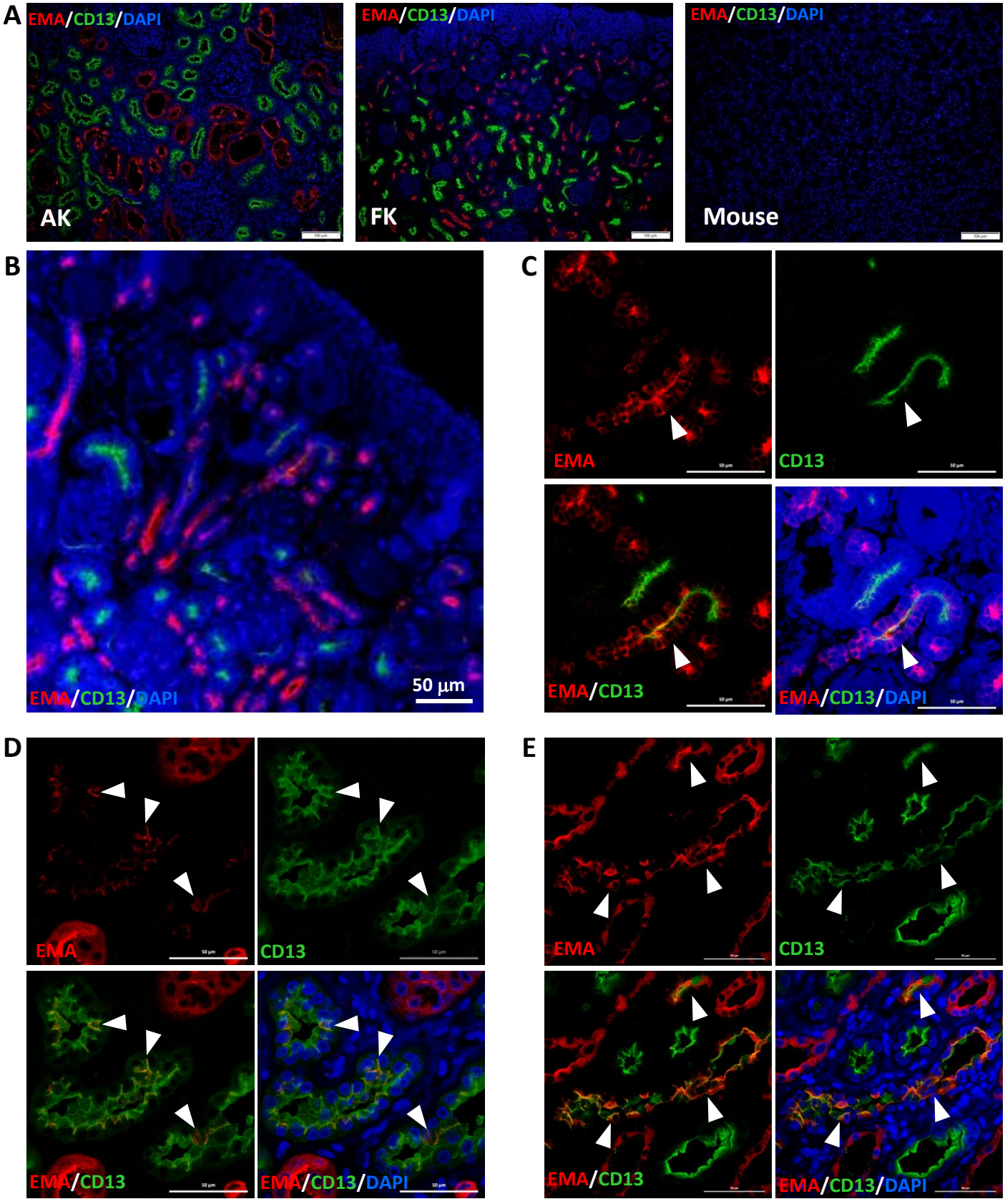

Figure S2: (A) Positive CD13 and EMA IF staining on human kidney tissue (adult and fetal), Negative staining on mouse kidney tissue. (B) Confocal microscopy images of human fetal kidney tissue, demonstrating the presence of tubule precursors, near the metanephric mesenchyme, which stain for both CD13 and EMA. (C) Higher magnification of (B), showing a double stained tubule. (D&E) Tubules in healthy human kidney tissues expressing both CD13 and EMA.

Figure S3: Tubulogenic engraftment potential of nSPH in the NOD/SCID mouse is diminished by hKEpC (Related to Figure 3)

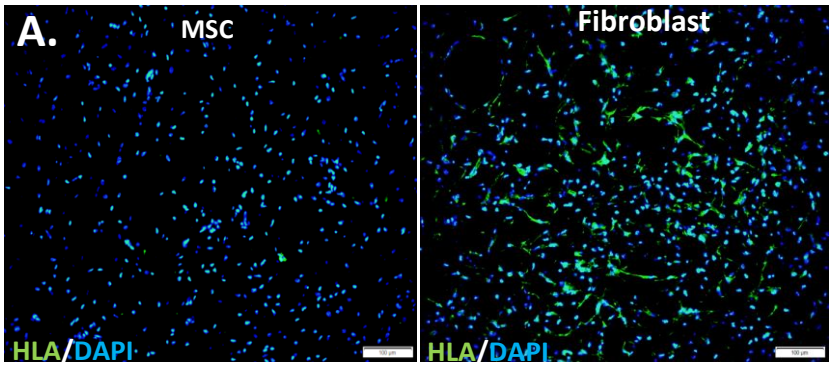

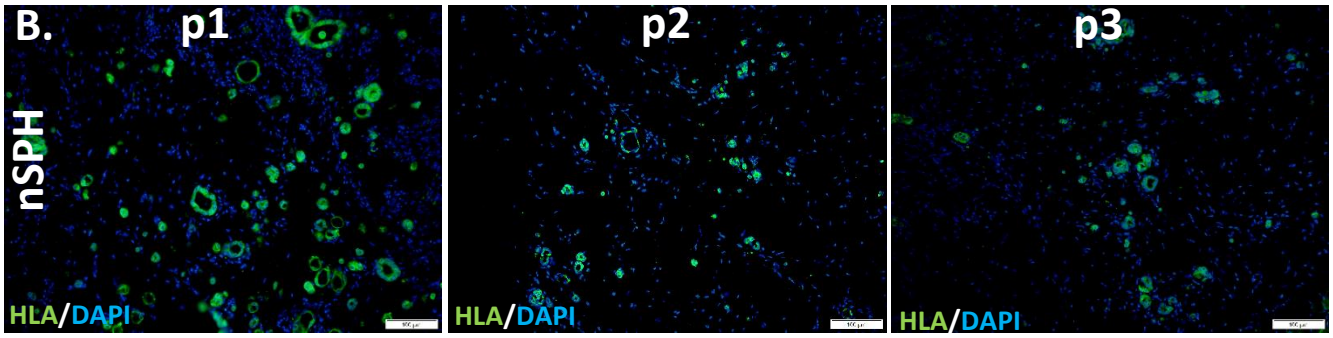

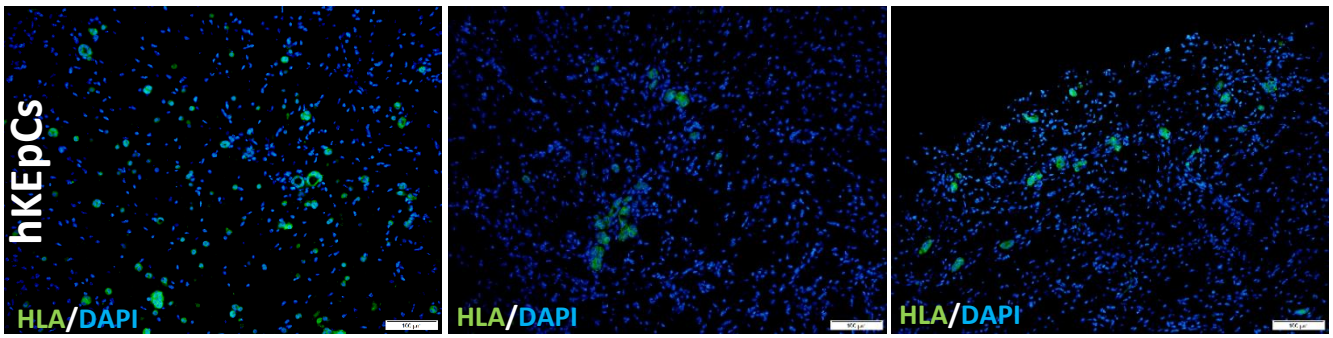

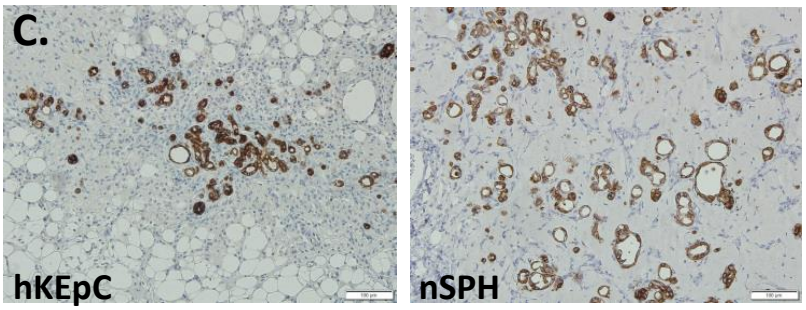

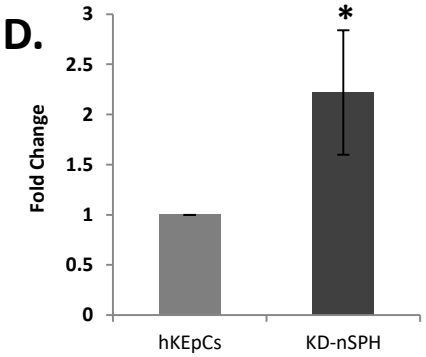

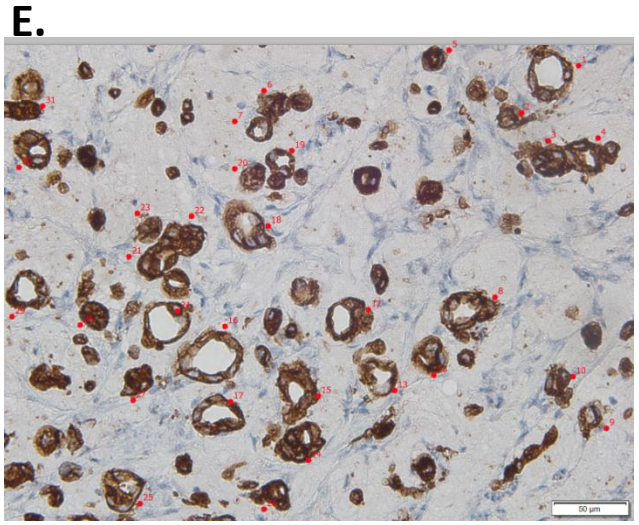

Figure S3: (A) MSC or fibroblasts lack the ability to form tubule-like structures upon subcutaneous cell injection of hKEpC into NOD-SCID mouse. (B) Tubule formation capacity of nSPH (upper panel) and hKEpCs (lower panel) derived from different passages, in the subcutaneous injection assay, showing progressive loss and overall cell survival in hKEpC grafts. (C) Both hKEpc and nSPH-derived cells generated tubule-like structure, as demonstrated by HLA staining. (D) Average number of tubules generated from hKEpCs and nSPH ($p=0.041$). (E) Method of structure counting (see materials and methods).

Figure S4: nSPH exert a beneficial functional effect in the cisplatin/UNx CKD mouse model (Related to Figures 5 and 6)

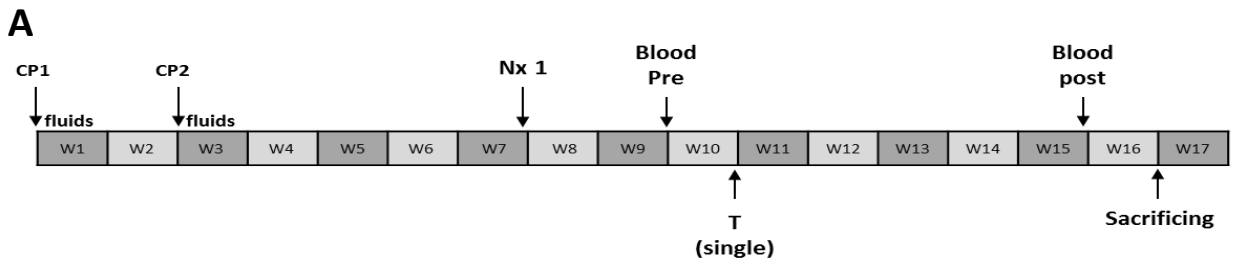

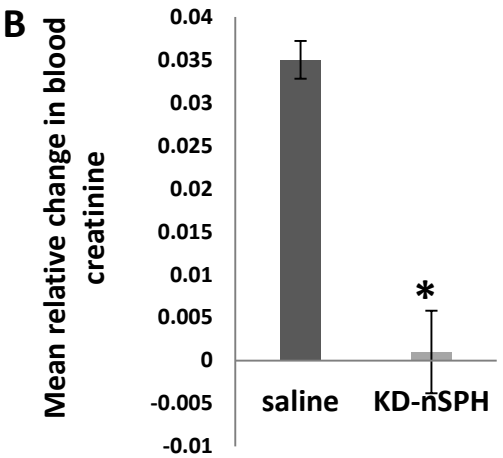

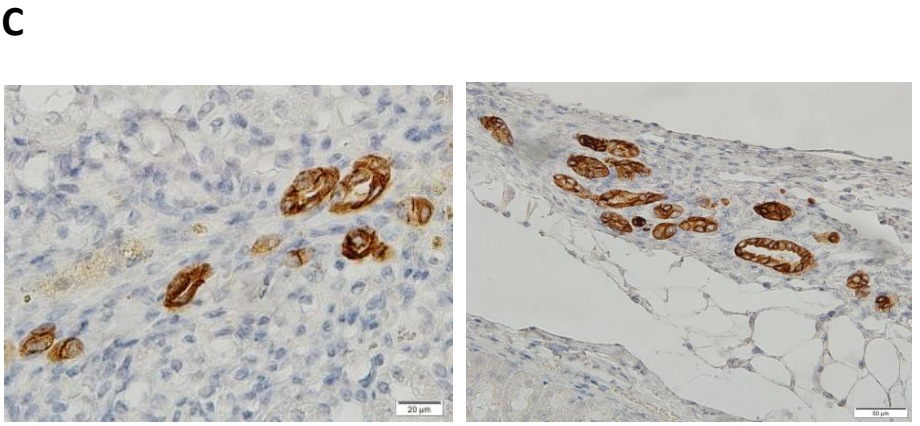

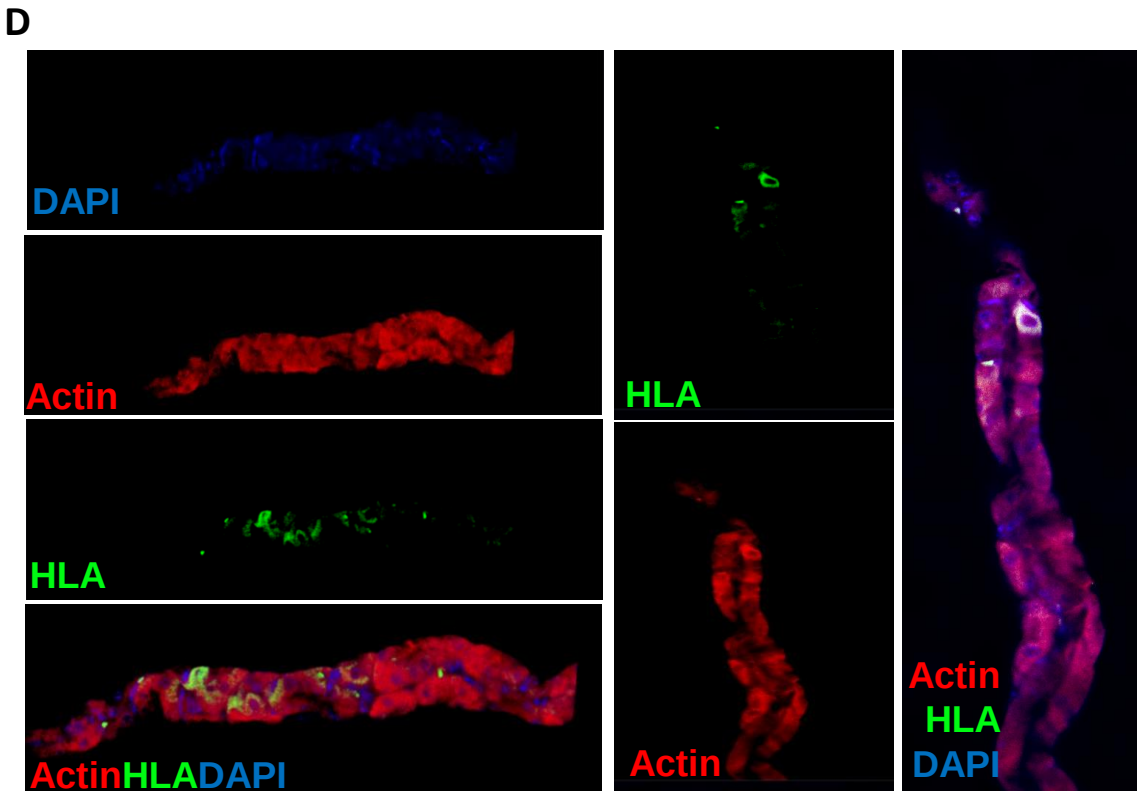

Figure S4: (A) Experiment scheme: First, NOD/SCID mice were subjected to two sets of intravenous (IV) Cisplatin (8mg/kg) (CP) administrations followed by a nephrectomy (Nx) procedure. Two weeks later, blood. Samples were collected to assess pre-treatment blood creatinine levels. 20 mice were randomly assigned for treatment with either nSPH (n=10) or saline (n=10), via intraparenchymal injections into the kidney. Blood was collected 4 weeks after treatment. Then, the mice are sacrificed, and the kidney remnant removed for histological analysis. (B) The Non-parametric Wilcoxon-Mann-Whitney Rank sum test for independent samples was applied to test the statistical significance of the difference in the relative change in Blood Cr at four weeks after transplantation compared to pre-transplantation, between the treatment (KD-nSPH) and control (Saline) groups. The change was found to be significantly lower in the SPH group compared to the saline group (P=0.0469). (C) HLA staining of the kidneys resected from nSPH-treated mice. Long-term engraftment of transplanted cells (>6-weeks post-transplant) as renal tubular structures was detected. (D) Confocal image of kidney tissue Immunostained with anti-HLA antibody and phalloidin (Actin) to mark grafted human cells. Cell nuclei are counterstained using DAPI. Dotted white lines demarcate mouse renal architecture.

Figure S5: hKEpC and nSPH derived from non-functional kidneys have similar *in vitro* characteristics to cells derived from functional kidneys (Related to Figure 7)

A.

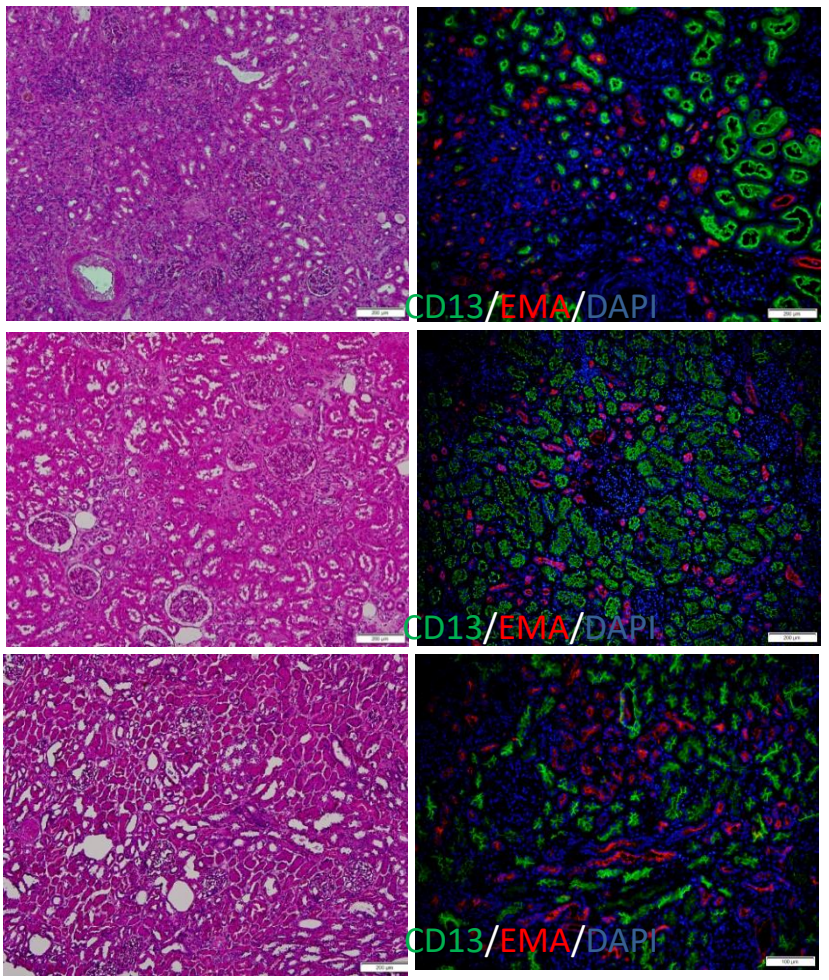

B.

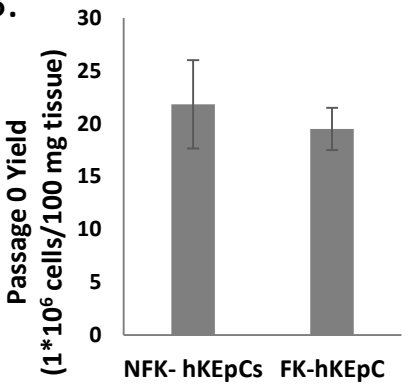

C.

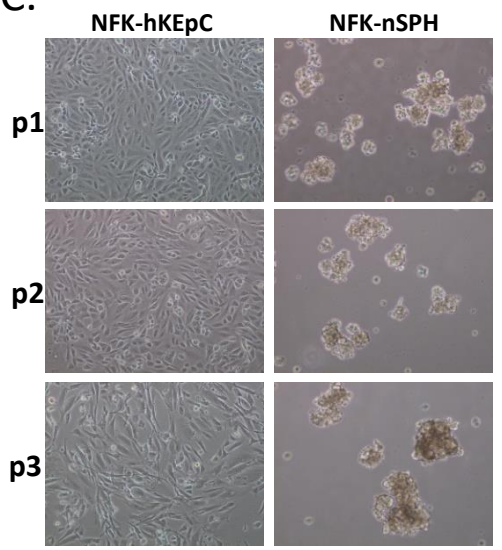

D.

Marker	Category	Culture Condition	Number	AVERAGE	SDEV
CD24	Epithelial	NFK-hKEpCs	5	99%	0.000
		NFK-nSPH	4	99%	0.000
CD105	MSC	NFK-hKEpCs	5	15.5%	0.120
		NFK-nSPH	4	1%	0.005
CD73	MSC	NFK-hKEpCs	5	100%	0.004
		NFK-nSPH	4	99%	0.000
CD90	MSC	NFK-hKEpCs	5	34%	0.230
		NFK-nSPH	4	11%	0.079
CD45	Hematopoietic	NFK-hKEpCs	5	1%	0.002
		NFK-nSPH	4	1%	0.006
CD31	Endothelial	NFK-hKEpCs	5	3%	0.008
		NFK-nSPH	3	3%	0.036

.E

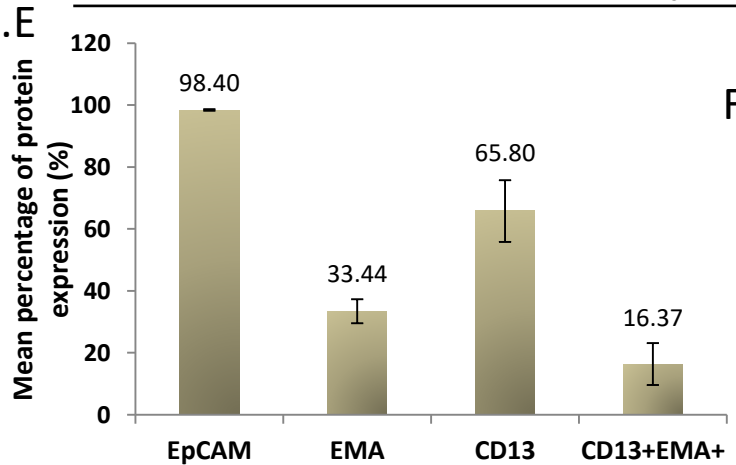

F.

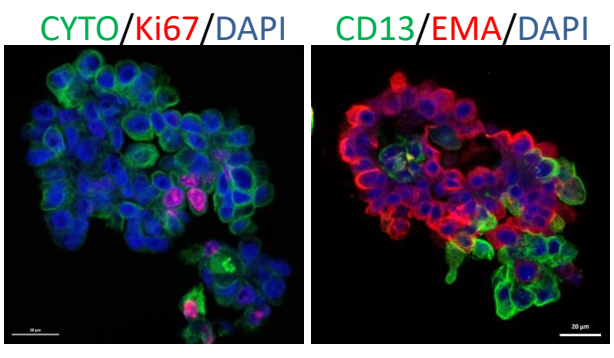

Figure S5: (A) Kidney tissues of three donors suffering from chronic kidney disease. Left: H&E staining. Right: Staining for the proximal and distal tubule markers (respectively): CD13 and EMA. (B) Number of cells yielded from 100mg tissue (n=5) of functional kidney-derived hKEpC (FK-hKEpC) and non-functional kidney derived-hKEpC (NFK-hKEpCs) (P=0.292). (C) NFK-hKEpCs exhibit similar morphology to FK-hKEpCs in both 2D and 3D conditions (X10 magnification). (D&E) Flow cytometry analysis of epithelial markers (EpCAM and CD24), mature kidney segment markers (CD13 and EMA), MSC markers (CD73, CD90 and CD105), the hematopoietic marker CD45 and the endothelial marker CD31 in NFK-hKEpCs and NFK-nSPH. Shown (E) is the percentage of cells expressing EpCAM (98.4%±2.4), the proximal and distal tubule markers CD13 (65.8%±9.9), and EMA (33.4%±3.9), respectively, and both CD13 and EMA (16.4%±6.8). (F) Confocal imaging of NFK-hKEpCs and NFK-nSPH stained for cytokeratin, the proliferation marker Ki-67 (left panel), CD13 and EMA (right panel).

Figure S6: hKEpC and nSPH derived from diseased and normal kidneys cluster together in PCA plots (Related to Figure 7)

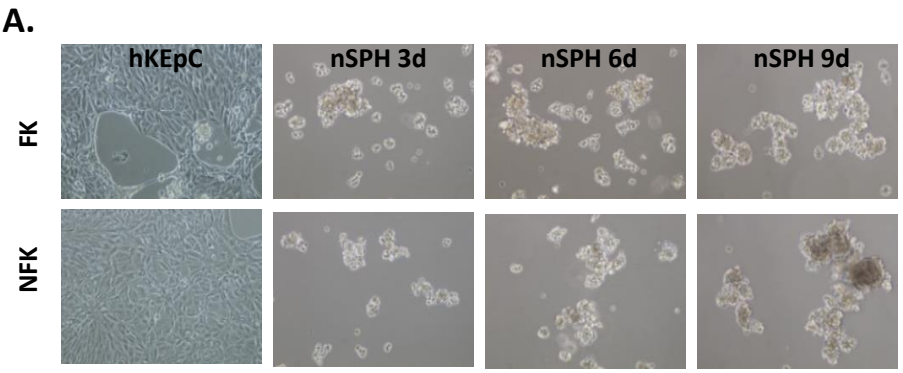

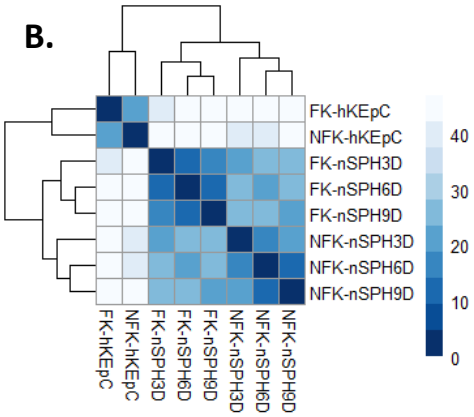

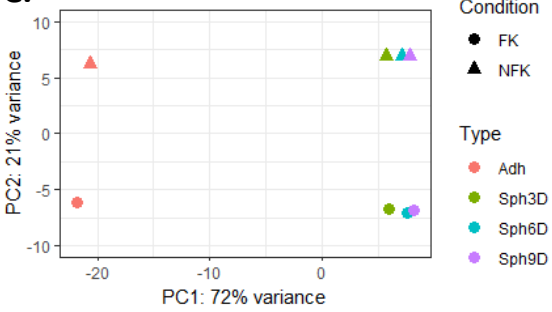

D.

Trend	Onthology	pValue	Bonferroni
Up regulation	tube morphogenesis (GO:0035239)	7.53E-07	7.60E-04
	tube development (GO:0035295)	1.85E-06	1.12E-03
	kidney development (GO:0001822)	6.88E-06	2.17E-03
	epithelium development (GO:0060429)	1.29E-05	3.16E-03
	renal system process (GO:0003014)	8.42E-05	6.04E-03
Down regulation	cell cycle (GO:0007049)	2.05E-18	7.98E-15
	mitotic cell cycle (GO:0000278)	4.83E-16	6.27E-13
	cell cycle process (GO:0022402)	7.55E-14	3.27E-11
	regulation of cell cycle (GO:0051726)	2.39E-12	5.47E-10
	regulation of cell proliferation (GO:0042127)	2.95E-11	6.39E-09

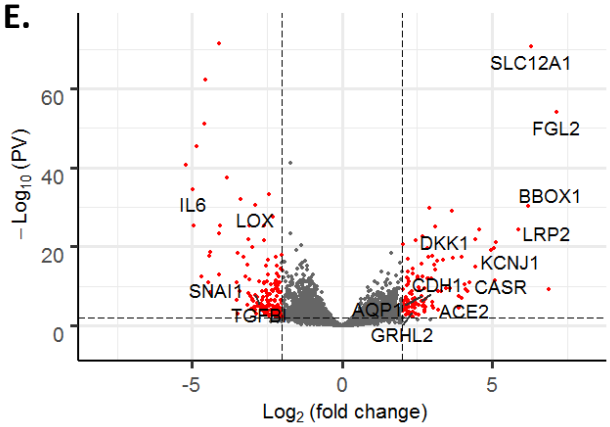

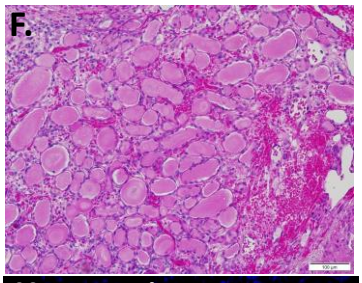

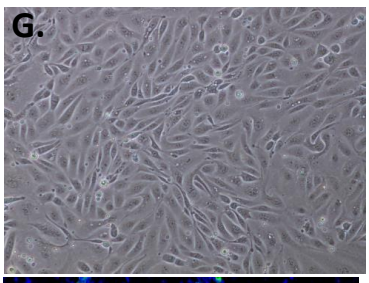

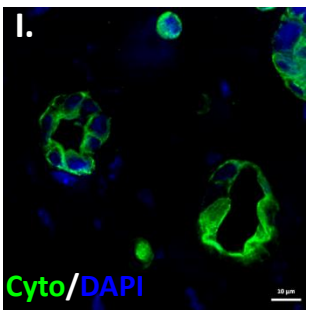

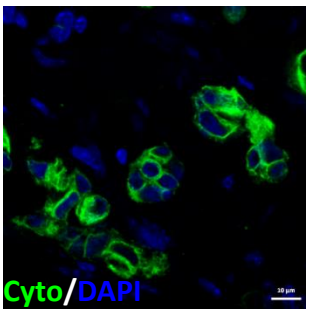

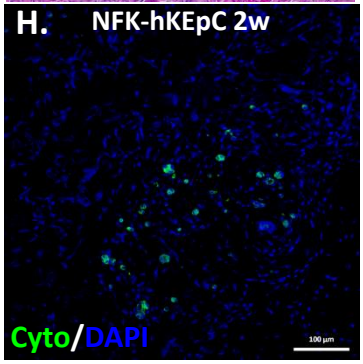

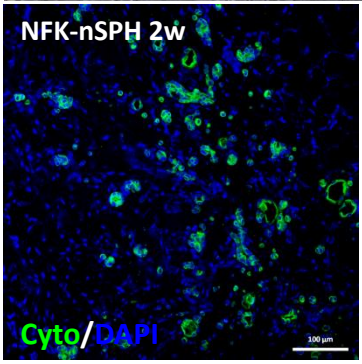

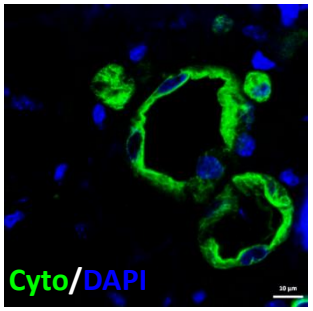

Figure S6: (A) Phase contrast microscopy images of FK-hKEpC, NFK-hKEpC and nSPH thereof, grown for 3, 6 and 9 days. Similar morphology is seen (X10 magnification). (B) Euclidean distance analysis was performed on RNA-seq data to illustrate variation in transcription levels between FK-hKEpC, NFK-hKEpC and nSPH thereof. The difference between cell types is demonstrated by a heatmap. While hKEpC are different from nSPH, FK-hKEpC and NFK-hKEpC are similar to each other and clustered together. There is greater similarity between FK-nSPH and NFK-nSPH grown for the same time period, in comparison to different time periods. Darker color indicates greater similarity. (C) Principal component analysis was preformed on RNA-seq data to illustrate variation in transcription levels between cultures in both functional and non-functional kidney derived cultures. Different colors denote culture condition. Different shapes denote if culture was derived from functional or non functional kidney. (D) Ontology analysis were conducted on deferentially expressed genes in nSph-day 6 in comparison to hKEpC derived from 4 kidneys. Ontology analysis revealed that up-regulated genes are related to kidney morphogenesis and development while down-regulated genes relate to cell cycle and cell proliferation. (E) Volcano plot demonstrating differentially expressed genes between day 6-nSPH and hKEpC derived from 4 kidneys. Red points denote differentially expressed genes with p-value<0.01 and Log2(fold change) >2 or <-2. log2 (fold change) is plotted on the x-axis, -log10(p-value) is plotted on the y-axis. (F-I) A patient's non-functioning end-stage kidney was resected ten years after he had started dialysis. Analysis of the native, non-functional kidney (NFK), from a patient who underwent renal transplantation: (F) H&E staining. (G) 2D culture generated from the kidney. (H) Staining of grafts generated by SC injecting 2D cultures or nSPH thereof, into NOD-SCID mice, following 2 weeks, for the epithelial marker cytokeratin (green). (I) Higher magnification of the structures in (H).

Figure S7: Renal epithelia from non-functioning kidneys are revitalized in nSPH (Related to Figure 7)

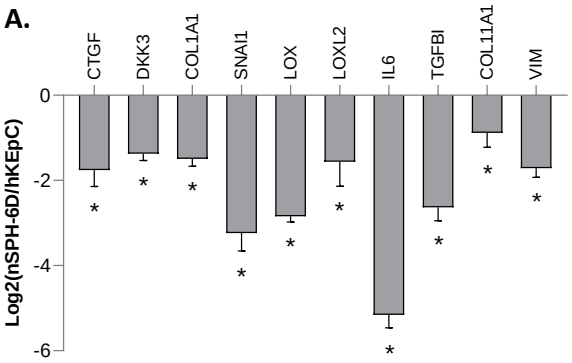

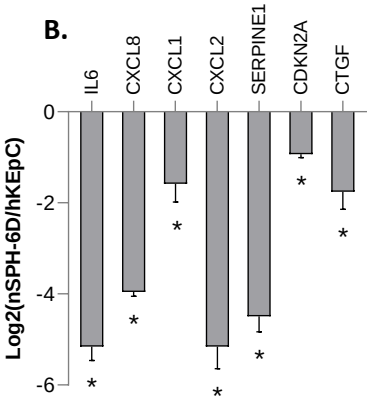

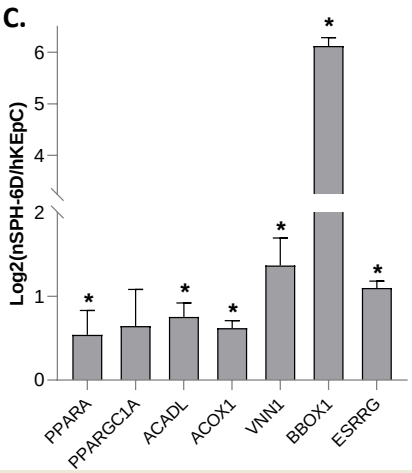

D.

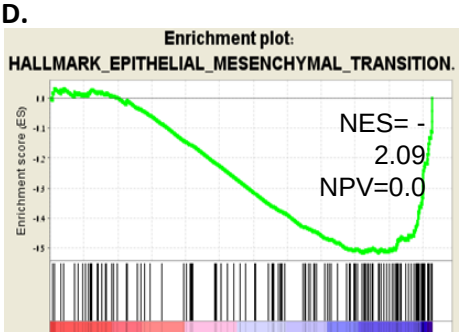

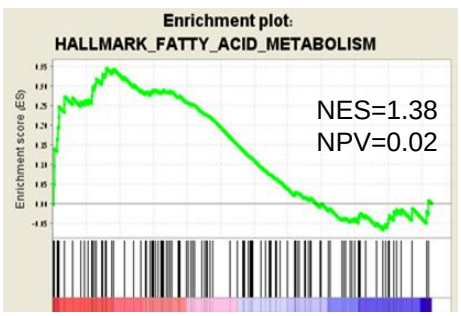

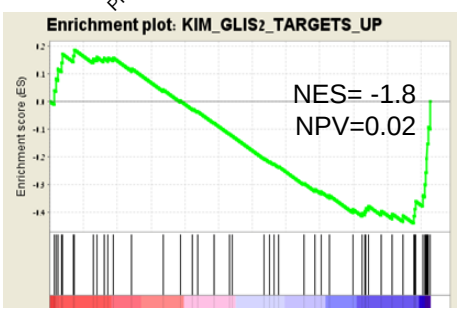

E.

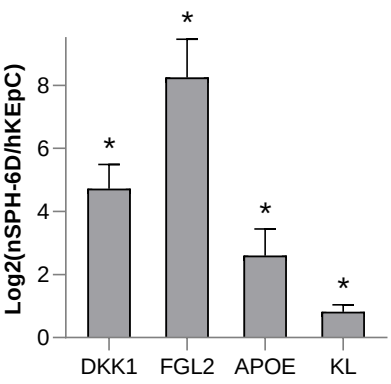

F.

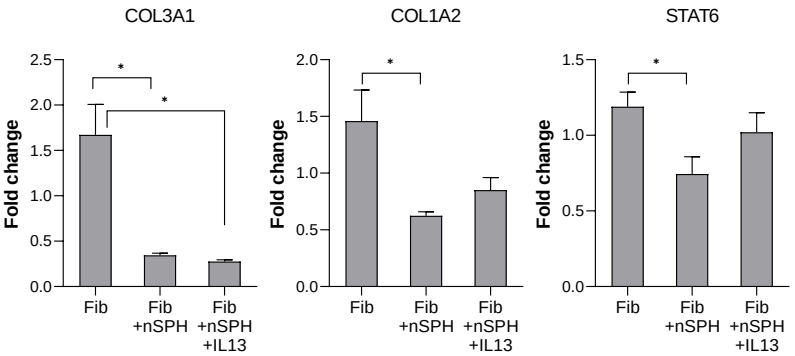

G.

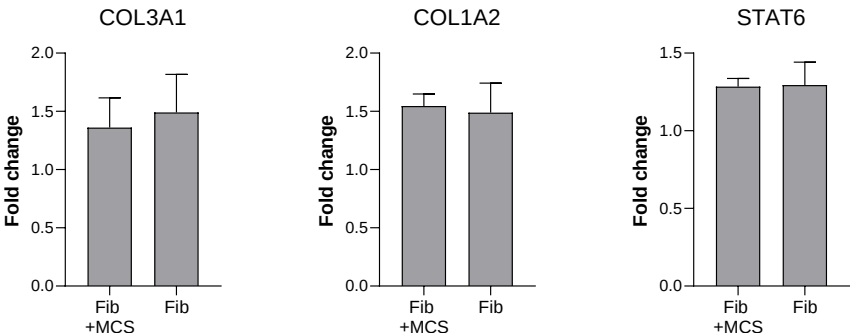

Figure S7: (A) RNA-seq analysis shows significant reduction of pro-fibrotic stress induced tubular epithelia-derived molecules in both FK-nSPH and NFK-nSPH in comparison to hKEpC (n=4; P<0.004, t-test). (B) RNA-seq analysis demonstrates significant down-regulation of senescence-associated secretory phenotype (SASP) molecules in both FK-nSPH and NFK-nSPH (n=4; p<0.005, t-test). (C) RNA-seq analysis demonstrates significant up-regulation of critical fatty acid (FA) oxidation molecules in both FK-nSPH and NFK-nSPH (n=4; P<0.005, t-test). (D) GSEA analysis of both FK-nSPH and NFK-nSPH transcriptomes revealed down-regulation of EMT and up-regulation of FA oxidation in nSPH. Genes up-regulated in the GLIS2 mutant mouse kidneys (mouse model of tubular atrophy, tubulo-interstitial fibrosis and terminal CKD) are down regulated in nSPH (E). RNA-seq analysis of secreted molecules, demonstrating significant up-regulation of the anti-fibrotic/inflammatory molecules *DKK1*, *FGL2*, *APOE* and *KLOTHO* in FK-nSPH and NFK-nSPH compared to hKEpCs. (F-G) Anti-fibrotic effects of nSPH in co-culture models. (F) qPCR analysis of fibroblasts grown with NFK-nSPH in the absence (Fib+nSPH) or presence of IL13 (Fib+nSPH+IL13) or without NFK-nSPH (Fib) for *COL3A1*, *COL1A2* and *STAT6* (*P<0.05) (G) qPCR analysis of fibroblasts grown with (Fib+MSCs) or without MSCs (Fib) for *COL3A1*, *COL1A2* and *STAT6*.

Figure S8: Activation of endogenous repair: PRC1 is significantly enhanced in host mouse tubules >1 month after nSPH transplantation (related to figures 6 and 7)

A

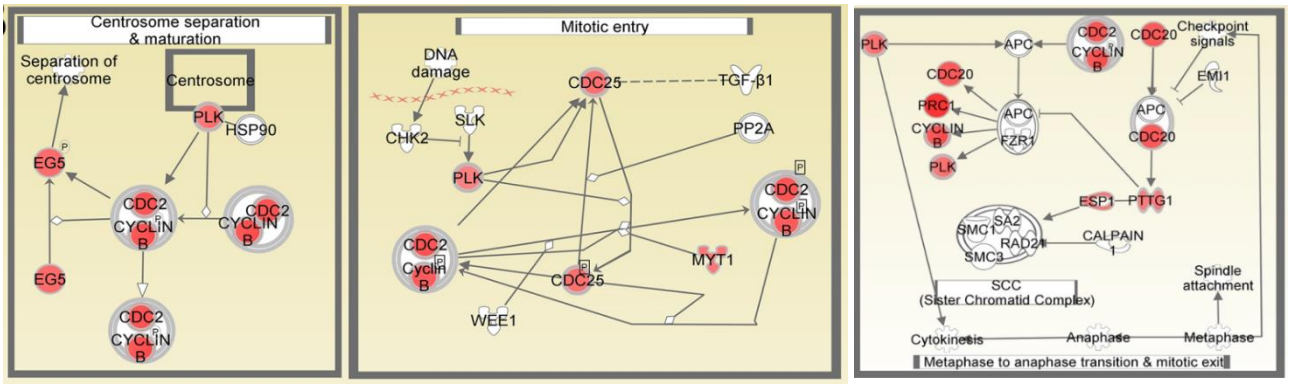

B

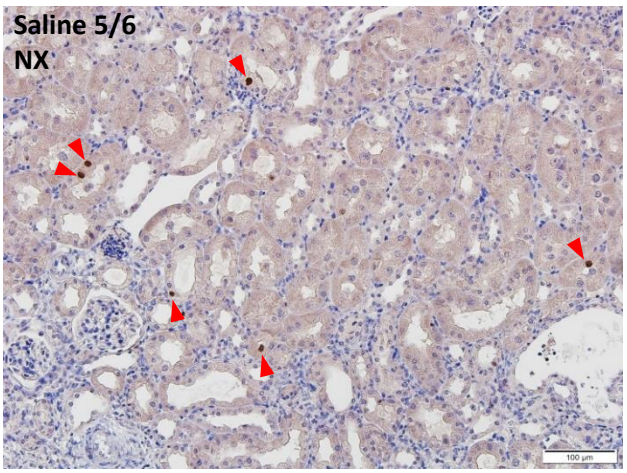

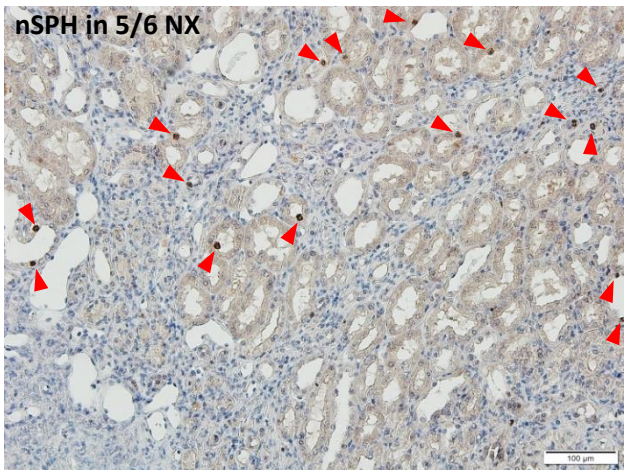

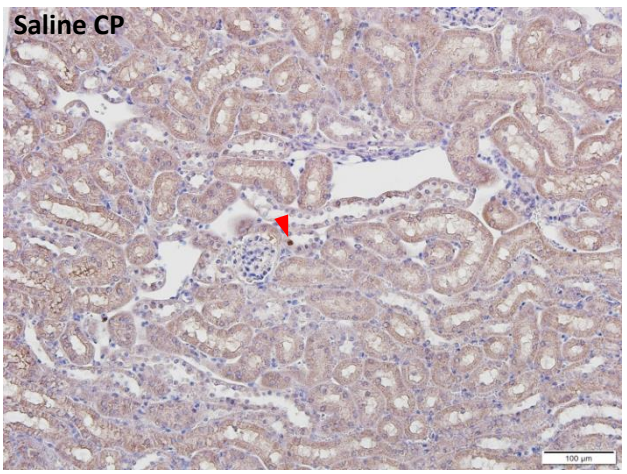

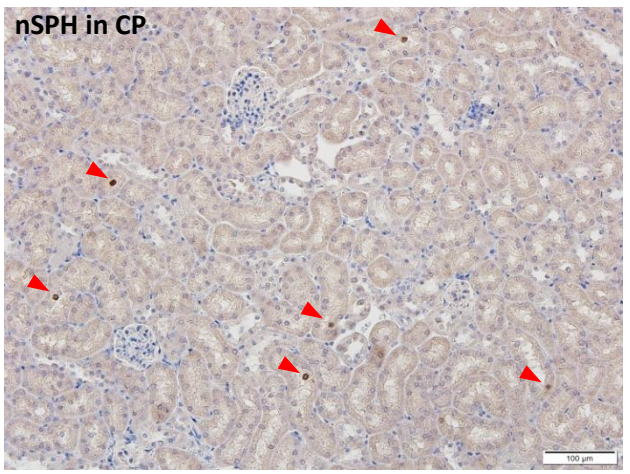

C

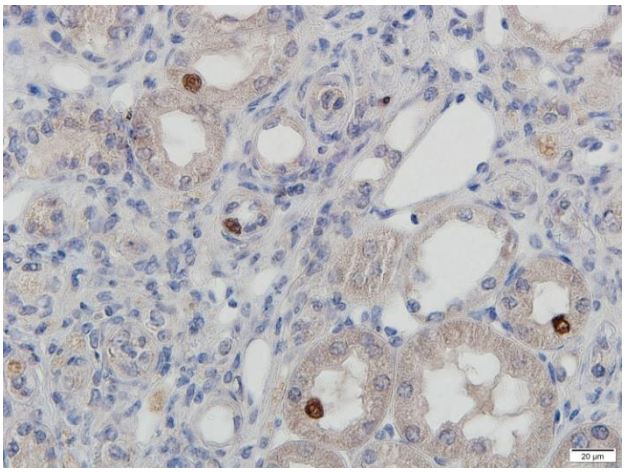

D

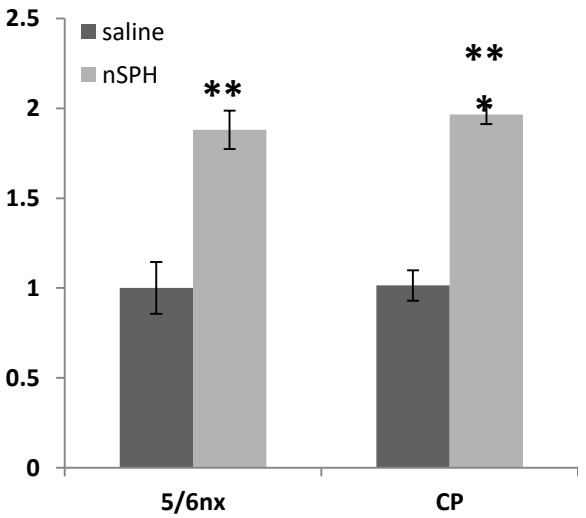

Figure S8: Using Ingenuity Pathway Analysis (IPA), we analyzed the transcriptomic effects of nephrospheres (nSPH) in mice with damaged kidneys. Molecules in red represent activated effectors. (A) Scheme of the mitotic roles of PLK1 pathway, the most significantly activated pathway, which exhibited a Z-score of 1.9 and a pValue of 10^{-12}. Note the significant up-regulation of PRC1. PRC1, which was significantly upregulated in the mouse transcriptome following nSPH treatment, is a positive regulator of G2/M exit. nSPH treatment results in PRC1 upregulation: (B) nSPH were administered into the kidneys of mice suffering from two types of kidney damage: 5/6 nephrectomy (Nx) and Cisplatin nephropathy (CP), and the kidneys were then stained for PRC1 (red arrows) in control (saline-treated, left) and nSPH-treated (right) mice 4-5 weeks after nSPH transplantation. (C) Higher magnification of nSPH-treated kidneys, demonstrating nuclear PRC1 expression in host mouse tubules. (D) Quantification of PRC1-expressing nuclei, demonstrating a significant increase in PRC1 expression in nSPH-treated vs. saline-treated mice, in both models of kidney damage (t-test, **P<0.005, ***p<0.00005).

Table S3: Surface marker expression in hKEpCs and nephrospheres (related to figure 2)

Marker	Category	Culture Conditions	Number	MIN	MAX	AVERAGE	SDEV
EpCAM	Epithelial	ADH	6	98%	99%	99%	0.0052
		SPH	8	90%	99%	96%	0.0392
CD24	Epithelial	ADH	5	96%	99%	98%	0.0000
		SPH	7	77%	99%	83%	0.0953
CD105	MSC	ADH	5	1%	15%	8%	0.0997
		SPH	7	1%	5%	3%	0.0186
CD73	MSC	ADH	6	99%	100%	99.8%	0.0071
		SPH	7	94%	100%	98%	0.0227
CD90	MSC	ADH	5	16%	67%	32%	0.0424
		SPH	7	1%	31%	11%	0.1025
CD45	Hematopoietic	ADH	5	0.50%	0.90%	0.7%	0.0016
		SPH	7	0.7%	1%	1%	0.0082
CD31	Endothelial	ADH	3	0.50%	1.70%	1%	0.0237
		SPH	3	0.7%	2.7%	1.9%	0.0266

Table S4: Blood creatinine levels in nSPH-treated and control mice (related to figure 5)

Relative change from pre-injection by treatment group and by time point

	SPH						saline					
Relative change in Blood Cr	*Post 1st injection*	*Post 2nd injection*	*Post 3rd injection I*	*Post 3rd injection II*	*Post 3rd injection III*	*Post 3rd injection (mean I-II-III)*	*Post 1st injection*	*Post 2nd injection*	*Post 3rd injection I*	*Post 3rd injection II*	*Post 3rd injection III*	*Post 3rd injection (mean I-II-III)*
N	42	39	31	18	14	31	36	32	26	15	8	26
Mean	2.41	-9.96	-17.95	-17.83	-41.95	-23.59	4.75	2.07	-10.45	-2.43	-36.00	-13.79
Std	22.5	28.0	21.1	19.7	20.6	18.3	28.1	36.5	22.1	39.3	17.6	23.0
Min	-40.9	-64.3	-63.0	-64.3	-68.8	-64.1	-47.2	-54.2	-53.6	-36.1	-61.0	-53.6
Median	3.0	-14.8	-13.5	-18.1	-46.1	-20.6	-5.0	-5.8	-10.9	-13.4	-31.9	-13.4
Max	89.3	66.7	18.8	11.1	8.4	5.4	73.6	116.0	40.3	123.2	-14.5	49.3
Lower 95% Confidence Limit	-4.59	-19.02	-25.71	-27.64	-53.84	-30.32	-4.76	-11.10	-19.38	-24.22	-50.69	-23.08
Upper 95% Confidence Limit	9.41	-0.90	-10.19	-8.03	-30.06	-16.87	14.26	15.24	-1.53	19.36	-21.31	-4.50
P-value from paired t-test	0.4903	0.0321	<.0001	0.0013	<.0001	<.0001	0.3178	0.7511	0.0236	0.8146	0.0007	0.0053

Repeated Measures Models-Relative change in Blood Cr

Type 3 Tests of Fixed Effects

Effect	*Num DF*	*Den DF*	*F Value*	*Pr > F*
Time point	4	84.7	23.59	<.0001
Treatment Group	1	199	4.85	0.0288
Donor	2	189	32.59	<.0001

Table S5: Creatinine clearance in nSPH-treated and control mice (related to figure 5)

Relative change from pre-injection by treatment group

	SPH						saline					
Relative change in CrCl	*Post 1st injection*	*Post 2nd injection*	*Post 3rd injection I*	*Post 3rd injection II*	*Post 3rd injection III*	*Post 3rd injection (mean I-II-III)*	*Post 1st injection*	*Post 2nd injection*	*Post 3rd injection I*	*Post 3rd injection II*	*Post 3rd injection III*	*Post 3rd injection (mean I-II-III)*
N	40	37	31	18	14	31	38	33	26	16	7	27
Mean	11.97	32.31	79.25	64.52	177.84	102.04	-2.97	13.70	41.70	13.09	104.90	53.55
Std	86.3	95.0	125.0	124.0	216.9	136.2	45.8	54.1	96.2	67.2	158.3	94.8
Min	-83.3	-56.6	-56.1	-67.1	-50.0	-56.1	-78.3	-91.3	-55.0	-75.0	-52.0	-54.2
Median	-12.4	6.7	28.6	40.1	80.1	32.7	-13.2	-3.3	13.6	9.2	46.5	42.4
Max	377.8	400.0	368.4	477.8	692.9	455.6	128.0	112.0	316.0	168.3	406.7	316.0
Lower 95% Confidence Limit	-15.64	0.64	33.41	2.87	52.61	52.06	-18.03	-5.48	2.86	-22.70	-41.55	16.06
Upper 95% Confidence Limit	39.57	63.99	125.10	126.17	303.07	152.02	12.09	32.89	80.54	48.89	251.35	91.04
P-value from paired t-test	0.3859	0.0458	0.0014	0.0413	0.0090	0.0002	0.6917	0.1553	0.0364	0.4477	0.1302	0.0069

Repeated Measures Models-Relative change in CrCl

Type 3 Tests of Fixed Effects

Effect	*Num DF*	*Den DF*	*F Value*	*Pr > F*
Time point	4	80.4	7.44	<.0001
Treatment Group	1	217	4.54	0.0343
Donor	2	200	8.36	0.0003

Table S6: Patient characteristics (related to figure 7)

	AGE	GENDER	Kidney Function (%)	CKD etiology
Donor 1	75	F	>2.5%	Ureteral tumor
Donor 2	54	F	>2.5%	Nephrolithiasis
Donor 3	87	M	>2.5%	Ureteral tumor
Donor 4	42	M	>2.5%	Reflux nephropathy
Donor 5	65	M	>2.5%	Iatrogenic ureteral stricture
Donor 6	76	M	>2.5%	Ureteral tumor
Donor 7	69	M	>2.5%	Ureteral tumor
Donor 8	51	M	>2.5%	Ureteral obstruction due to rectal cancer
Donor 9	58	M	8%	Ureteropelvic junction obstruction
Donor 10	71	F	>2.5%	Hypertension
Donor 11	71	M	>2.5%	Nephrosclerosis due to hypertension
Donor 12	76	M	>2.5%	Nephrolithiasis
Donor 13	78	F	>2.5%	Ureteral obstruction due to uterine cancer
Donor 14	55	F	>2.5%	Nephrolithiasis
Donor 15	57	F	>2.5%	Nephrolithiasis